Highlights

The Role of Continental Heterogeneity on the Evolution of Continental Plate Margin Topography at Subduction Zones

Antoniette Greta Grima, Thorsten W. Becker

- We investigate continental heterogeneity using free-surface subduction models
- Continental structure modulates OP topography, extension, trench and slab dynamics
- Variations in back-arc basin properties reflect variations in continent structure

In press at EPSL, June 2024.

The Role of Continental Heterogeneity on the Evolution of Continental Plate Margin Topography at Subduction Zones

Antoniette Greta Grima[a], Thorsten W. Becker[b,c,d]

[a]*School of Geographical and Earth Sciences, University of Glasgow, School of Geographical and Earth Sciences, University of Glasgow, Molema Building, Lilybank Gardens,, Glasgow, G128QQ, United Kingdom*
[b]*Institute for Geophysics, Jackson School of Geosciences, The University of Texas at Austin, J.J. Pickle Research Campus, Bldg. 196 10100 Burnet Road, Austin, TX 78758-4445, Texas, USA*
[c]*Department of Earth and Planetary Sciences, Jackson School of Geosciences, The University of Texas at Austin, 2275 Speedway Stop C9000, Austin, Austin, TX 78712-1722, Texas, USA*
[d]*The Oden Institute for Computational Engineering & Sciences, The University of Texas at Austin, 201 E 24th Street, Austin, Austin, TX 78712-1229, Texas, USA*

Abstract

The nature of the overriding plate plays a major role for subduction zone processes. In particular, the highly heterogeneous continental lithosphere modulates intra-plate tectonics and the surface evolution of our planet. However, the role of continental heterogeneity is relatively under-explored for the dynamics of subduction models. We investigate the influence of rheological and density variations across the overriding plate on the evolution of continental lithosphere and slab dynamics in the upper mantle. We focus on the effects of variations in continental plate margin and keel properties on deformation, topographic signals, and basin formation. Our results show that the thickness, extent, and strength of the continental plate margin and subcontinental

In press at EPSL, June 2024.

keel play a crucial role for the morphology and topography of the overriding plate, as well as the retreat of the subducting slab. We show that this lateral heterogeneity can directly influence the coupling between the subducting and overriding plate and determine the partitioning of plate velocities across the overriding plate. These findings suggest that back-arc extension and subsidence are not solely controlled by slab dynamics but are also influenced by continental plate margin and keel properties. Large extended back-arc regions, such as the Pannonian and Aegean basins, may result from fast slab rollback combined with a weak continental plate margin and a strong and extended continental keel. Narrow margins, like the Okinawa Trough in NE Japan, may indicate a comparatively stronger continental plate margin and weaker or smaller continental keel. Additionally, continental keel properties may affect the overall topography of the continental lithosphere, leading to uplift of the deformation front and the formation of intermontane basins.
Keywords: continental plate margin topography, continental heterogeneity, back-arc extension, subduction zone evolution

1. Introduction

The presence of an overriding, continental lithosphere at subduction zones is a key feature of modern-day plate tectonics and exerts a first-order control on subduction zone evolution, trench rollback, slab dip angle at the trench, and hence slab morphology on the top of the lower mantle (e.g. Capitanio et al., 2010; Butterworth et al., 2012; Sharples et al., 2014; Holt et al.,

2015a,b; Crameri and Lithgow-Bertelloni, 2018). Relative to oceanic lithosphere, continental plates consist of thick, buoyant crust resisting recycling and geologically stable regions are often underlain by strong, depleted mantle lithosphere and surrounded by weak, deformable margins (e.g. Jordan, 1981; Lenardic et al., 2000). Results from geopotential, seismic, tomographic, geochemical, and rock physics studies show great variability in chemical and rheological composition, thickness, temperature, density, extent, and age across the continental lithosphere from its margin to its interior domains, with implications for continental deformation, plate boundary weakening, surface mobility and plate tectonics in general (e.g. Jordan, 1981; Ghosh et al., 2010; Audet and Bürgmann, 2011; Pearson et al., 2021).

Continental cratons or "roots", make up a major component of the continental lithosphere and these are understood to be old, thick, cold, and chemically distinct due to their fractionation (Jordan, 1981; Lee et al., 2005). For a planet with active plate tectonics, cratons are intriguing in that they have resisted subduction through many Wilson Cycles. This implies continents have to be neutrally or positively buoyant,and also relatively high viscosity, to resist recycling (Lenardic et al., 2000, 2003; Rolf and Tackley, 2011; Yoshida, 2012). Deeply penetrating roots underneath cratonic shields can increase the coupling between the lithosphere and the mantle and modify the surface deformation style (Zhong, 2001; Conrad and Lithgow-Bertelloni, 2006; Becker, 2006; O'Driscoll et al., 2009; Yang and Gurnis, 2016; Paul et al., 2023).

Continental plate margins outside cratons are regions of high strain rates, accommodating within their deformation most of the relative plate motions (e.g. Gordon, 2000; Zhong, 2001; Becker, 2006; Ghosh et al., 2013; Yang and Gurnis, 2016). At subduction zones such margins record the history of subduction and deformation (Uyeda, 1982). Based on estimates of upper plate strain derived from the type of earthquake focal mechanisms, Heuret and Lallemand (2005) and Lallemand and Heuret (2017) broadly classified the deformation of the overriding plate margin into either back-arc extension or compression. Previous work suggests that this dichotomy of back-arc behaviour may be governed by subduction parameters, such as the convergence velocity, trench rollback, the direction of motion of the overriding plate, the degree of plate coupling at the trench (determined by the strength of the subduction interface), the subducting plate age and the angle of subduction (Sleep and Toksöz, 1971; Chase, 1978; Molnar and Atwater, 1978; Heuret et al., 2007; Sdrolias and Müller, 2006; Sternai et al., 2014; Sharples et al., 2014).

Significant numerical and analogue modelling efforts have sought to better understand the role of the continental lithosphere at subduction zones. The problem can be approached from a global, mantle flow perspective (e.g. Naliboff et al., 2009; Ghosh et al., 2013; Yang and Gurnis, 2016; Paul et al., 2023), or with a regional perspective which makes it easier to capture the temporal evolution of the margin with high resolution (e.g. Capitanio et al., 2010; Butterworth et al., 2012; Sharples et al., 2014; Holt et al., 2015a,b;

Crameri and Lithgow-Bertelloni, 2018; Wolf and Huismans, 2019).

Here, we build on the efforts of O'Driscoll et al. (2009), Manea et al. (2012), and Taramón et al. (2015) to investigate the impact of weak continental margins and strong cratons on subduction dynamics. Specifically, we explore the effects of variations in continental plate margin and keel properties on the evolution of deformation, topographic signal, and basin formation in a 2-D numerical model of subduction with and without a free surface boundary condition. Expanding on the back-arc deformation studies for a homogeneous overriding plate by Balázs et al. (2017), Wolf and Huismans (2019), Dasgupta et al. (2021), and Erdős et al. (2022) we show that continental deformation and back-arc extension can occur in both wide and narrow continental back-arcs, and is controlled to a large extent by the thickness, extent, and strength of the continental plate margin and the continental keel. The nature of this heterogeneity influences the extent, asymmetry of deformation and subsidence within the back-arc region, and the amount of trench retreat on the subducting plate.

2. Methods

2.1. Modelling approach

We model freely evolving subduction and interactions with an overriding plate within the approximation of a thermo-mechanical, 2-D convective system (Holt et al., 2015a; Holt and Condit, 2021). For this, we use the finite element code ASPECT (version 2.3.0) (Kronbichler et al., 2012; Heister

In press at EPSL, June 2024.

et al., 2017; Bangerth et al., 2021) to solve the equations for the conservation of mass (eq. 1), momentum (eq. 2) and energy (eq. 3) for incompressible, laminar flow, with Boussinesq approximation and no internal heating:

$$\nabla \cdot \mathbf{v} = 0 \tag{1}$$

$$-\nabla \cdot (2\eta\dot{\epsilon}) + \nabla p = \rho \mathbf{g} \tag{2}$$

$$\left(\frac{\partial T}{\partial t} + \mathbf{v} \cdot \nabla T\right) - \kappa \nabla^2 T = 0 \tag{3}$$

Here, v is the velocity, $\dot{\epsilon}$ is the strain-rate tensor, η viscosity, p pressure, g gravitational acceleration, ρ density, T temperature, and κ thermal diffusivity. Our basic setup builds on Holt and Condit (2021), and Table 1 provides more details on the model parameters used in this study.

2.1.1. Numerical parameters and boundary conditions

Our model domain extends 11,600 km in the x-direction and 2,900 km in the y-direction (Fig. 1). Side and bottom boundaries are free slip and our top boundary is a free surface which allows for self-consistent mesh deformation and topographic build-up with model evolution. We also include model suites with a mechanical free slip top boundary condition (bc) to compare the role of the free surface in the evolution of overriding plate topography and slab dynamics (Table A.4 and Figs. A.9-A.12). For our free surface models, we

In press at EPSL, June 2024.

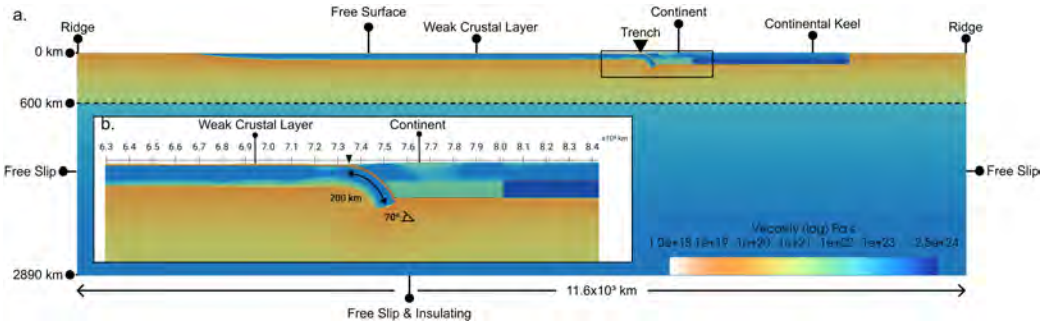

Figure 1: a) Model set-up with a free surface top boundary condition and a continental keel with inset, b), showing a zoomed-in view of the subducting and overriding plates, the weak crustal layer, and the initial condition at the start of our models for reference-keel case 4.

advect the free surface in the direction of the surface normal (instead of that of the local vertical) to avoid mesh distortions and better mass conservation preservation of the domain. We also apply a diffusion process in order to counteract the strong mesh deformation, similar to Sandiford et al. (2021). We limit our initial maximum time step (to 200 years), the relative increase in time step (to 20), and the overall maximum time step allowed in the model (to 2,000) to encourage initial isostatic convergence to equilibrium.

We use ASPECT's adaptive mesh refinement (AMR) to increase the resolution of our models around the subducting slab, at the top of the model domain, within the overriding continental lithosphere and around and within a 7.5 km thick weak crust which acts as an interface between the subducting and overriding plates. We do this by setting AMR to occur for finite elements with large gradients in viscosity, temperature, and composition. This allows us to obtain a resolution of 500 m to 1 km within the regions of interest while also modelling flow at the scale of the whole mantle. For models

with a free surface top boundary condition, AMR is initiated after the first 0.5 Myr of model evolution to avoid recurring refinement during the free surface oscillations prior to its isostatic stabilisation.

2.1.2. Initial conditions

The initial set-up for our reference case model (keel-free case 1, Table A.4) includes a 6,000 km long, 80 Ma old oceanic lithosphere subducting at an initial subduction angle of 70°, with a slab length of 200 km, under a 2500 km long, 150 km thick, 120 Ma, buoyant continental lithosphere (Table 1). Both the oceanic and continental plates are bounded by ridge segments on either side of the model domain and are separated by a 7.5 km thick weak crustal layer (Fig. 1). This crustal layer has viscosity of 10^{20} Pa s and acts to decouple the two plates where the properties of the crustal layer were discussed by Behr et al. (2022).

To test the role of continental heterogeneity on the evolution of subduction and topography, we compare our keel-free case 1 model with our reference-keel case 2 where we implement a 75 km thick, 200 km long keel at the bottom of the continental lithosphere (Fig. 1). The continental keel starts at 200 km away from the edge of the continental lithosphere at the trench and extends all the way under the remaining extent of the overriding plate. In our models, the keel strength is represented by a viscosity increase from 10^{23} Pa s (i.e., the standard viscosity of the continental lithosphere in our models) to 10^{24} Pa s. The weak crustal layer, the continental overriding

In press at EPSL, June 2024.

plate, and the continental keel are implemented and advected as separate compositional fields, which are discussed next.

2.1.3. Temperature and density structure

The lithospheric plates in our models are based on half-space cooling for 80 Ma and 120 Ma age, respectively. The density in our models is temperature dependent and we include different reference densities for the background mantle and oceanic lithosphere, the overriding continental plate and continental keel, and the oceanic crust (Table 1). In the reference-keel cases (cases 2 and 4), the continental plate and continental keel have the same density but this is modified for some specific test cases (Table A.4). The crust and the overriding plate material have lower densities compared to the oceanic lithosphere and mantle which is to ensure a positively buoyant continental plate and to approximate the lower density of the basaltic crust similar to the approach adopted by Behr et al. (2022).

In press at EPSL, June 2024.

Parameter	Symbol	Units	Value
Thermal expansion coefficient	α	K^{-1}	$3 \cdot 10^{-5}$
Thermal diffusivity	κ	m^2s^{-1}	10^{-6}
Surface temperature	T_s	K	273
Mantle potential temperature	T_m	K	1573
Adiabatic temperature gradient	d_zT	K km^{-1}	0.3
Slab and mantle density	ρ_0	kg m^{-3}	3300
Weak Crust density	ρ_{crust}	kg m^{-3}	3175
Continental and keel density	ρ_{op}	kg m^{-3}	3150
Gravitational acceleration	g	m s^{-2}	9.8
Subducting plate age	t_{sp}	Myr	80
Subducting plate viscosity	η_{sp}	Pa s	$2.5 \cdot 10^{22-23}$
Weak Crust viscosity	η_{crust}	Pa s	$2.5 \cdot 10^{20}$
Weak Crust thickness	h_{crust}	km	7.5
Overriding plate age	t_{op}	Myr	120
Overriding plate viscosity	η_{sp}	Pa s	$2.5 \cdot 10^{22-23}$
Overriding plate thickness	h_{op}	km	150
Reference keel viscosity	η_{keel}	Pa s	$2.5 \cdot 10^{24}$
Reference keel thickness	h_{op}	km	75
Maximum viscosity	η_{max}	Pa s	$2.5 \cdot 10^{24}$
Minimum viscosity	η_{min}	Pa s	$2.5 \cdot 10^{18}$
Dislocation creep (UM)			
Activation energy	E	$kJmol^{-1}$	540
Activation volume	V	cm^3mol^{-1}	12
Pre-factor	A	$Pa^{-1}s^{-1}$	$8.5 \cdot 10^{-15}$ (LM)
Exponent	n	-	3.5
Diffusion creep (UM,LM)			
Activation energy	E	$kJmol^{-1}$	300 (UM,LM)
Activation volume	V	$cm^3mol{-}1$	4 (UM), 2.5 (LM)
Pre-factor	A	$Pa^{-1}s^{-1}$	10^{-10} (UM), $5.78 \cdot 10^{-13}$ (LM)
Exponent	n	-	1
Plastic yielding			
Friction coefficient	a	-	0.6
Cohesion	b	MPa	60
Pore fluid factor	λ	-	0.15
Maximum yield stress	τ_{max}	MPa	600

Table 1: Model parameters

In press at EPSL, June 2024.

2.2. Rheology

We use a composite creep law combining diffusion creep, dislocation creep, and plastic yielding (e.g. Billen and Hirth, 2005; Becker, 2006; Garel et al., 2014). For the upper mantle, we use the following creep laws:

$$\eta_{diff/disl} = A^{\frac{1}{n}} \dot{\epsilon}_{II}^{\frac{1-n}{n}} \exp \frac{E + PV}{nRT}, \tag{4}$$

Where η is the composite viscosity, A a pre-factor, $\dot{\epsilon}_{II}$ the second invariant of the strain rate tensor, n the stress exponent, R the gas constant, P the lithostatic pressure, and T temperature. Our choices of parameters (Table 1) are consistent with experimental values for olivine (e.g. Hirth and Kohlstedt, 2004). We include a 0.3°C km^{-1} adiabatic temperature gradient for T in eq. (4), and set the diffusion and dislocation creep pre-factors to give η_{diff} = $\eta_{disl} = 5 \cdot 10^{20}$ Pa s at a transition strain rate of $5 \cdot 10^{-15}$ s^{-1} and depth of 330 km (*cf.* Billen and Hirth, 2005; Becker, 2006). We increase the viscosity of the lower mantle by a factor of 20 as motivated by geoid constraints (e.g. Hager, 1984; King and Masters, 1992) and limit deformation in the lower mantle to occur only through diffusion creep.

We include quasi-plastic behavior by approximating brittle yielding at lithospheric depths, defined as

$$\eta_{yield} = \frac{\min(\tau_{yield}, 0.5\text{GPa})}{2\dot{\epsilon}_{II}}, \tag{5}$$

In press at EPSL, June 2024.

where τ_{yield} is approximated by a Coulomb friction criterion

$$\tau_{yield} = (a\sigma_n + b)\lambda. \tag{6}$$

Here, a is the friction coefficient (0.6), b is the cohesion (60 MPa), λ is the pore fluid factor also known as the yielding pre-factor and is defined as (e.g. Enns et al., 2005)

$$\lambda = 1 - \frac{P_{fluid}}{P_{rock}} \tag{7}$$

For our reference model λ has a value of 0.15 but we increase this to 0.3 and decrease it to 0.07 for our reduced and increased plastic yielding cases respectively (Table A.4). Similar to previous work we assume that σ_n is equal to the lithostatic pressure P.

The effective viscosity is then calculated as

$$\eta_{eff} = \left(\frac{1}{\eta_{diff}} + \frac{1}{\eta_{disl}} + \frac{1}{n_{yield}} \right)^{-1} \tag{8}$$

and is additionally bounded between an upper limit of $2.5 \cdot 10^{24}$ and a lower limit of $2.5 \cdot 10^{18}$ Pa s to encourage model convergence.

2.3. Model parameters and variations

We compare our keel-free case 1 and our reference-keel case 2 (sec. 2.1.2) against variations in continental lithosphere strength. We first include a 75 km weak layer at the bottom of the continental lithosphere (keel-free case 3) to approximate a rheologically weaker lower continental crust. Next, for keel-

case 4 we combine this weaker lower continental lithosphere with a strong continental keel. This set-up describes a continental plate margin with a weak lower continental crust and a continental interior underlain by stronger continental lithosphere. For cases 1-4 we test each set-up using a free surface and a free slip top boundary condition (Table A.4).

To explore the effect of the continental keel properties on the evolution of topography and slab morphology we then vary the properties of the continental keel by changing its thickness (cases 5 and 6), extent (case 7), density (case 8), and viscosity (cases 9 and 10; Table A.4). We also vary the margin properties by decreasing the keel-free margin extent (case 11), varying its thickness (case 12), and changing the amount of yielding allowed (cases 13 and 14; Table A.4).

2.4. Model analysis

For each model we track; i), the average overriding and subducting plate velocities (measured within the plate core and averaged over the length and depth of the plate), ii), the convergence velocity, iii), the velocity of the sinking slab and the induced return flow in the upper mantle, iv), the viscosity, stress, strain rate, and temperature evolution, and, v), the topographic evolution.

We also measure the slab dip angle θ at 175 km depth

$$\theta = \tan^{-1} \frac{\delta y}{\delta x}, \tag{9}$$

In press at EPSL, June 2024.

where δy is the depth measured between 175 km at the surface and the slab tip if this is above 400 km depth or at 400 km depth if the slab tip has sunk into the mantle transition zone. δx describes the horizontal distance between the top of the slab at 175 km depth and the slab tip.

The velocity V_{tr} of the subducting plate at the trench is defined here as the deepest point on the subducting plate located away from the ridge and is described by:

$$V_{tr} = \frac{V_{stokes}}{\tan\theta}, \tag{10}$$

where V_{stokes} is the vertical velocity of the slab measured directly from the model output and θ is the slab dip angle at 175 km depth (eq. 9).

We also define a deformation extent (Δ DE) within the overriding plate. This describes the keel-free margin of the continental lithosphere. For this region, we track the change in horizontal extent, strain rates, and viscosity from the model output. Our convergence rate is calculated based on the velocity of the subducting lithosphere, the trench, the deformation region, and the velocity of the continental craton (defined as that part of the continental lithosphere overlying by the continental keel). We also track the amount of trench rollback (Δ TR) for every 0.5 Myr of model time. Lastly, we qualitatively examine the slab morphology within the upper mantle and at 660 km depth.

In press at EPSL, June 2024.

3. Results

3.1. Surface boundary conditions, topography, and dynamics

Since we seek to evaluate topography predictions, we test a range of model set-ups (Table A.4) with both a free surface and a free slip top boundary to compare the influence of the boundary condition on the slab morphology, the strain rates and the topography generated on the overriding plate (Fig. A.13 and Table A.3). In terms of deep dynamics, there is little variation in the slab angles (Table A.3) and general slab morphology irrespective of the surface boundary conditions are used (Fig. A.9 - A.12), as expected (Kaus et al., 2008).

For keel-free case 1 and keel-case 2, continental strain rates and surface topography are also comparable save for minor, small-scale features (Figs. A.13, A.9-A.10 and Table A.3). In keel-free case 1 both the free surface and free slip implementations record a topography decrease from 4.5 to 3 km in the first 30 Myrs which decreases by an other 0.5 km over the next 30 Myrs, after which elevations drop by an additional 0.5 km until the model ends at 100 Myrs. The main difference between these cases is that latter shows an offset basin subsidence ranging from 3...2.5 km in the first 31 Myr which deepens to an average constant depth of 2 km. The offset basin is bound by higher elevations of 4 - 3.5 km on either side for the first 31 Myrs. By model end time at 100 Myrs, the elevation of the basin shoulders drops by an additional 0.5 km. Continental plate margin strain rates for keel-case 2 and keel-free case 1 are similar across both models and top boundary conditions

In press at EPSL, June 2024.

for the entire model run and the upper mantle stages of the slab sinking (Table A.3).

However, when introducing vertical and lateral heterogeneity within the overriding continental plate in keel-free case 3 and keel-case 4, the type of surface boundary condition becomes important for surface deformation (measured here as a function of strain rates and basin depth and width). For these cases the free surface implementation shows higher strain rates within the continental lithosphere for the first 30 Myrs of model evolution (cf. Crameri and Lithgow-Bertelloni, 2018) (case 3: $5.3 \cdot 10^{-16}$ s^{-1} for free surface vs. $4.2 \cdot 10^{-16}$ s^{-1} free slip and case 4: $5.4 \cdot 10^{-16}$ s^{-1} for free surface vs. $2.5 \cdot 10^{-16}$ s^{-1} free slip) and produces significantly different topographic signals compared to the free slip version of the same set-up (Fig. A.13) with free slip. In case 3 both free surface and free slip set-ups record elevations of 5 km across the entire continental lithosphere for the first $\sim$ 15 Myr. Elevation decreases rapidly in the following 15 Myrs (from 5to 3 km) and stabilise around 3...2.5 km between 25...60 Myr. Continental topography continues to decrease after 60 Myr to an average of 2 km for the free slip case and 1.5 km in the free surface case. However, in the free surface implementation, the high topography (5 km) observed in the first 15 Myrs is interrupted by five basins with depths ranging from 4...3.5 km. Between 17 and 47 Myrs these coalesce in to two basins which are 1 km deeper than the surrounding topography, and eventually merge into a 470 m wide basin that is 1 km deep and bound on either side by elevations of 2 km. Basin presence is coincident

with higher strain rates within the continental plate margin ($5.3 \cdot 10^{-16}$ s^{-1}). Both topographic behaviour and increases in strain rates are missing for the same model set-up with a free slip top boundary condition (Fig. A.11 and Table A.3).Case 4-free surface develops a well defined central zone of subsidence at 6 Myr with a depth 4 km and shoulder elevations of 4.5 km. The central basin topography drops with time until it reaches a depth 0.5 km with basin shoulder elevation of 2 km at 100 Myrs. In this case too, basin formation and subsidence mirror higher strain rates within the continental overriding plate margin (Fig. A.12 and Table A.3). The free slip version shows more subdued topography, indicating that while slab deep dynamics are comparable, the more involved free surface treatment may be required for more detailed topography analysis (Figs. A.13, A.12), and will hence be adopted subsequently.

3.2. Keel variations

Comparing keel-free case 3 and keel-case 4 (Figs. A.11 vs. A.12) it is clear that the presence of a higher viscosity continental keel underneath the continental interior makes an important contribution to the return flow within the upper mantle, the slab morphology, the location of deformation and the overall evolution of topography on the overriding plate. The keel in case 4 encourages strain rate focusing within the continental plate margin, resulting in a centralized zone of subsidence bounded by two shoulders of higher topography on either side of the margin, mimicking "horst" and "graben"

structures. This topographic signal forms early on in the model and is maintained through the model evolution. However, does the nature of the lateral heterogeneity introduced by the continental keel matter? To answer this question we vary the geometry and the rheology of the continental keel and compare the topographic signal, the strain rates within the continental plate and the slab morphology.

3.2.1. Geometry variations

Increasing the continental keel thickness (case 5, Fig. 2 and Table A.4) results in similar model behaviour and topographic signal. However, the subsidence within the central basin of the continental plate margin for this case, is both narrower (125 km vs. 130 km) and deeper (3.5 km vs. 3 km) compared to that observed for case 4 (Table 2). Decreasing the continental keel thickness (case 6) results in a significantly steeper slab overall ($\sim 70^{\circ}$ vs. the mean slab angle, $\sim 60^{\circ}$) and a reduced trench retreat (475 km vs. 860 km for case 4). Case 6 has no basins, limited margin subsidence of 1.5 km and a continental interior elevation change of 1 km over the model evolution (Fig. 2, Table 2). Maintaining a standard keel thickness and extending its length in case 7 (Fig. 2) encourages slab tip flattening at 660 km depth. A significant subsidence of 3.5 km within the continental plate margin results, and a wide deformation front (890 km) forms. The margin deformation is characterised by a central zone of extension split into 3 zones of subsidence which merge into one basin averaging a subsidence of 3 -3.5 km. This zone

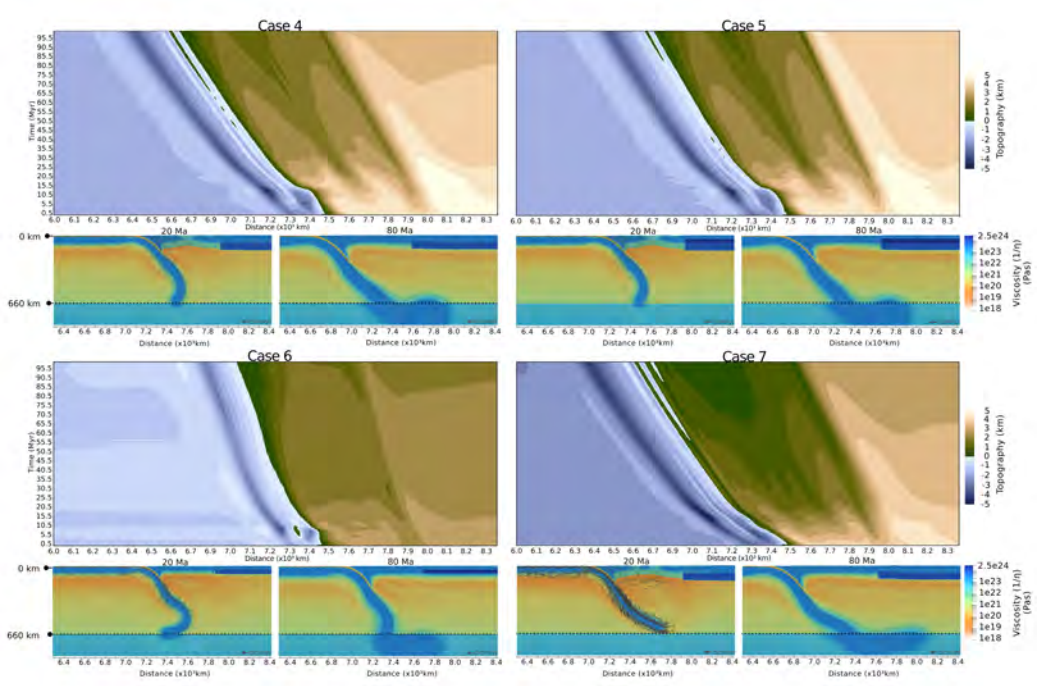

Figure 2: Effect of continental keel geometry: case 4 (top left) with standard keel; case 5 (top left) with thick keel; case 6 (bottom left) with thin keel; case 7 (bottom right) with wide keel. Layout and subplots are similar to Fig. A.13, but we now show viscosity and flow velocity at different timesteps in the small subpanels.

of extension (Table 2) is bounded by two areas with an elevation of 1 km higher than the subsided basin, similar to previous models with the same or thicker keel (cases 4 and 5).

3.2.2. Rheology variations

We next maintain the same keel geometry, but change its density in case 8 and viscosity in case 9 (Fig. 3 left and central panels and Table A.4). Introducing a continental keel with a higher density (Table A.4), results in an isostatically elevated deformed continental plate margin, with horsts that

are 5 km high and a subsided (1.5...1 km) continental interior. Despite the inversion of the typical topographic signal between the margin and the continental interior we still observe a focused center of subsidence (total of 3 km) within the continental plate margin. At its deepest (after a subsidence of 3 km) the central basin of case 8 is narrower compared to previous models (150 km vs. 190 km for case 4 and 300 km for case 8) but it is similarly bound by two horsts which are 1.5 km more elevated than the basin (Fig. 3 and Table 2).

In case 9 we maintain the reference keel density but increase its viscosity by two orders of magnitude (Table A.4). The margin topography is similar to that of cases 4, 5, 7, and 8 with a typical graben (with a subsidence of 3.5 km) flanked by elevated horsts. Both cases 8 and 9 show similar slab behaviour in the upper and lower mantle which is consistent with that observed for previous cases (Fig. 3 and Table 2).

Lastly, in case 10 we combine the extended keel of case 7 with the higher viscosity keel of case 9. We note very similar behaviour to case 7 with the development of an extensive and wide deformation front (440 km) along the continental plate margin. Similar to case 7, case 10 also exhibits multiple basins within a central zone of subsidence along the plate margin. These are the deepest basins recorded across all models with a subsidence of 4.5 km. Case 10 undergoes 710 km of trench rollback which produces slab flattening at 660 km depth. The slab eventually sinks below 660 km depth at 60 Myrs which coincides with a secondary phase of subsidence across the two basins

In press at EPSL, June 2024.

within continental plate margin (Fig. 3).

3.3. Margin variations

3.3.1. Geometry effects

We next vary the properties of the continental plate margin. For case 11 (Fig. 4) we decrease the margin extent and maintain the standard keel properties of case 4 (Fig. 2, Table A.4). The narrower margin is more deformed than in previous cases, with multiple basins evolving into 3 narrow and long basins at 45 Myr. This model has the steepest slab morphology ($\sim 80°$) from all models for the same upper mantle stage (Table 2). Combining a thin margin and keel (case 12, Fig. 4) results in smooth overriding plate topography where the overall elevation change across 100 Myrs of model evolution is just 1.5 km. Case 12 also lacks regions of uplift and basin nucleation common to the previous cases. The smooth and overall shallow topography (maximum topography reaches 3 km at model start and drops to 1.5 km after 76 Myr) is similar to the topographic signal recorded in case 6 (Fig. 2) and both cases show limited margin extent (50 km for case 12 vs. 75 km for case 6) and trench rollback (580 km for case 12 and 475 km for case 6). Case 12 shows transient, minor subsidence of 0.5 km along a narrow ledge between the margin and the continental keel, a steep slab ($\sim 74°$ in the upper mantle stages and 61° for the whole model run), and limited trench rollback of 580 km (Table 2, Fig. 4).

In press at EPSL, June 2024.

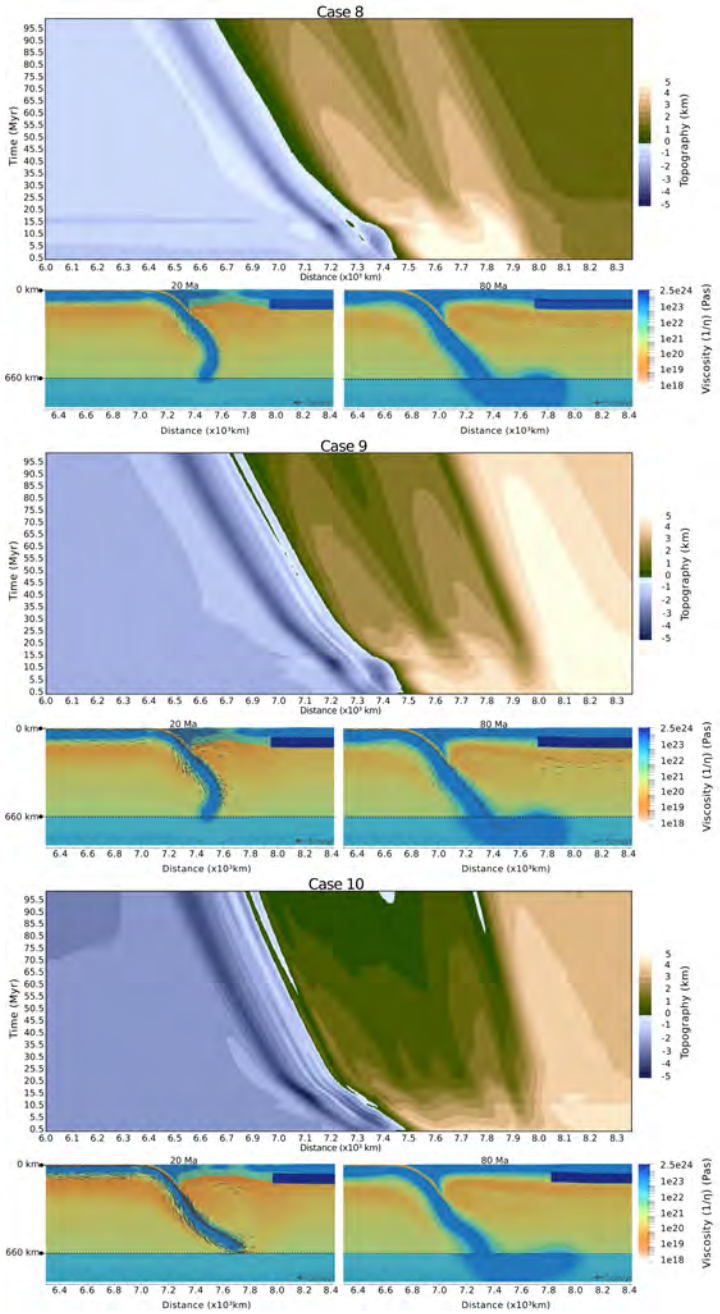

Figure 3: Effect of continental keel rheology: case 8 (top) with a neutrally buoyant keel; case 9 (centre) with a higher η of 10^{26} Pa s keel and case 10 (bottom) with an extended, 900 km, 10^{26} Pa s η keel. Top row: Topography; bottom row: viscosity and induced viscous flow velocity

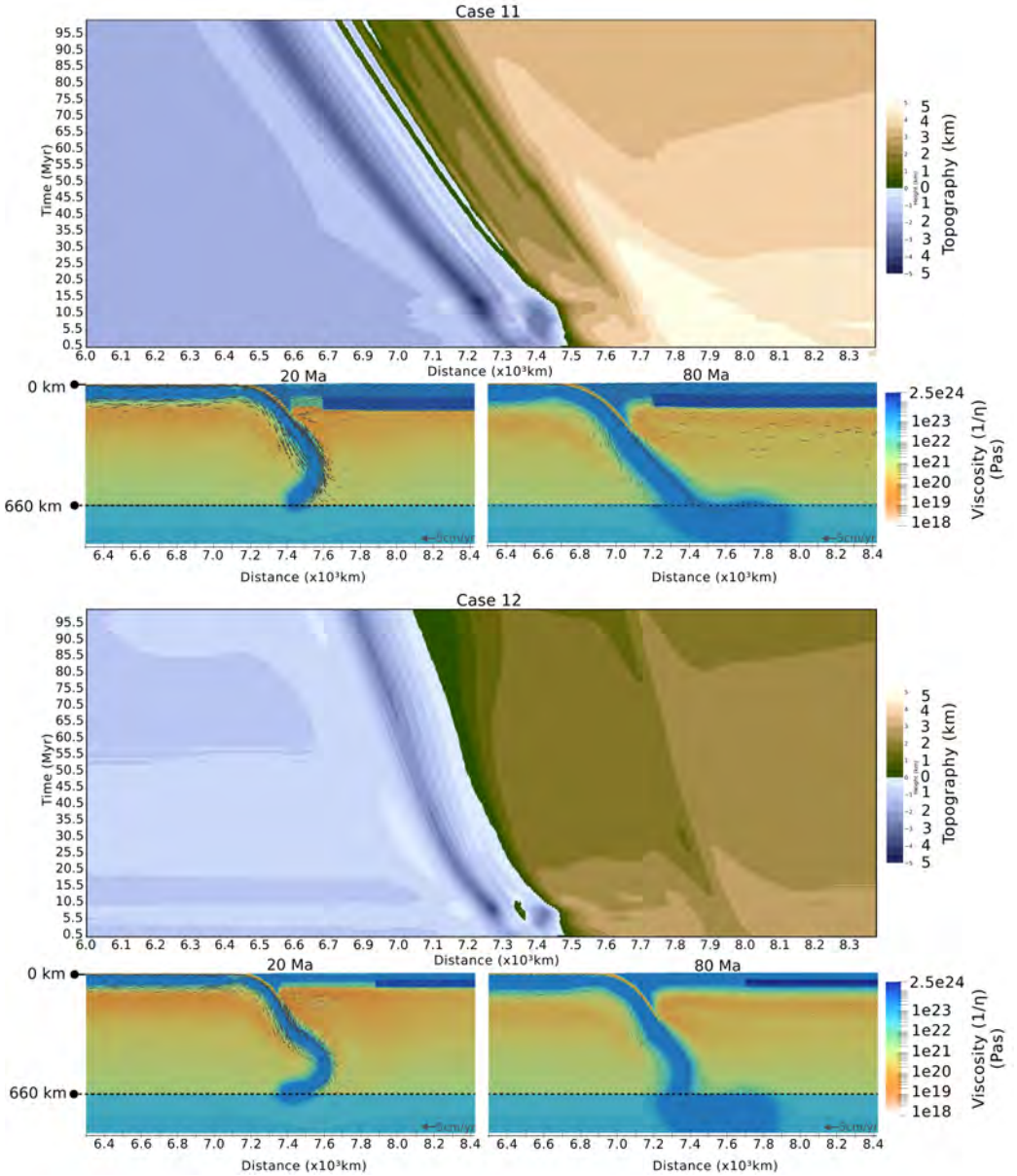

Figure 4: Effect of continental plate margin geometry: case 11 (top) with a narrow margin and standard continental keel; case 12 (bottom) with thin margin and keel. Top row and bottom row same as Fig.3

In press at EPSL, June 2024.

3.3.2. Rheology effects

We next test the effect of rheology (Fig. 5). Models have a standard keel but for case 13 the amount of plastic yielding allowed within the continental lithosphere (excluding the keel) is reduced by changing λ from 0.15 to 0.3 (cf. Enns et al., 2005). In case 13, an overall high topography of 5...4.5 km within the continental plate margin complements the elevated (5 km) continental interior for the first 15 Myrs of model evolution (Fig. 5). After 20 Ma the topography within the margin flattens from 5 km to 3...1.5 km and after 50 Myrs multiple narrow zones of focused subsidence ~ 0.5 km deeper than the surrounding topography develop. A consistent depression with a subsidence of 2 km also develops at 1 Myr within the continental plate margin at the edge of the keel shoulder (Fig. 3 and Table 2). Contrary to the subsidence in previous models this is confined the keel-ward edge of the margin (Fig. 4). Despite the different margin topography the slab evolution is similar to that observed for cases 4, 5, 8 and 9 (Fig. 5, Table 2).

In case 14 (Fig. 5) we increase the amount of plastic yielding allowed within the continental lithosphere (excluding the continental keel) by decreasing λ from 0.15 to 0.07. Increased plastic yielding results in an extended continental plate margin (430 km wide) with 3.5 km of subsidence. Subsidence is focused within two main basins which are bound by three horsts which are between 0.5-1 km higher than the basins they separate and bind on either side. The slab angles and morphology mimic that of cases 7 and 10 with deflection above 660 km and eventual descent into the lower mantle

Model	Margin Subsidence (km)	Margin Extent (km)	Number of Margin Basins	Interior Elevation Change (km)	Trench Depth (km)	Trench Rollback (km)	Slab Angle* Whole Model (∘)	Slab Angle Upper Mantle (∘)	Strain Rates Whole Model (s^{-1})	Strain Rates Upper Mantle (s^{-1})
Case 4	3	130	1	1.5	4	860	54.9	73.5	$2.1 \cdot 10^{-16}$	$5.4 \cdot 10^{-16}$
Case 5	3.5	125	1	1	3.25	790	56.1	73.5	$2.2 \cdot 10^{-16}$	$5.6 \cdot 10^{-16}$
Case 6	1.5	75	0	1	2.5	475	70.4	63.8	$1.2 \cdot 10^{-16}$	$3.7 \cdot 10^{-16}$
Case 7	3.5	360	3	1.5	4	890	56.7	66.3	$2.4 \cdot 10^{-16}$	$7.6 \cdot 10^{-16}$
Case 8	3	310	1	1.5	3.3	760	58.6	75.4	$2.2 \cdot 10^{-16}$	$5.8 \cdot 10^{-16}$
Case 9	3.5	320	3	1	3.7	725	57.1	74.0	$2.3 \cdot 10^{-16}$	$5.7 \cdot 10^{-16}$
Case 10	4.5	440	3	1	3.2	710	60.2	67.2	$2.6 \cdot 10^{-16}$	$7.9 \cdot 10^{-16}$
Case 11	2.5	60	3	1.5	3.8	755	56.6	77.9	$2.3 \cdot 10^{-16}$	$5.8 \cdot 10^{-16}$
Case 12	1	50	0	1	3.1	580	60.9	74.2	$9.8 \cdot 10^{-17}$	$2.5 \cdot 10^{-16}$
Case 13	3	195	6	1.5	3.3	805	56.0	77.8	$1.7 \cdot 10^{-16}$	$3.8 \cdot 10^{-16}$
Case 14	3.5	430	2	1.5	3.9	990	55.0	62.5	$2.8 \cdot 10^{-16}$	$9.3 \cdot 10^{-16}$

Table 2: Subduction parameters for models with keel (cases 4-10) and margin variations (cases 11-14). *Slab angles are measured at 175 km depth using eq. 9. Note: number of basins refers to the basins at the end of the model run and interior elevations change refers to the change in elevation of the continental interior (above the continental keel) from start to end of model.

after 60 Myr (Fig. 5, Table2).

3.4. The influence of continental heterogeneity on trench retreat and the extent of continental plate margin deformation

Heterogeneity in the continental lithosphere thus influences the morphology and topography of the overriding plate, and the trench retreat of the subducting lithosphere. Keel geometry and rheology can play a role on both the extent and amplitude of the deformation experienced by the continental plate margin. Fig. 6 shows the amount of trench retreat (ΔTR) against the area of deformed and wide continental plate margin (ΔDE) for all keel variations, for the whole model evolution (top), and the upper mantle stages (bottom). There is a linear relationship between the increasing trench retreat and the increase in deformation extent along the continental plate margin (Fig. 6). Comparing model evolution across the entire model run, models

In press at EPSL, June 2024.

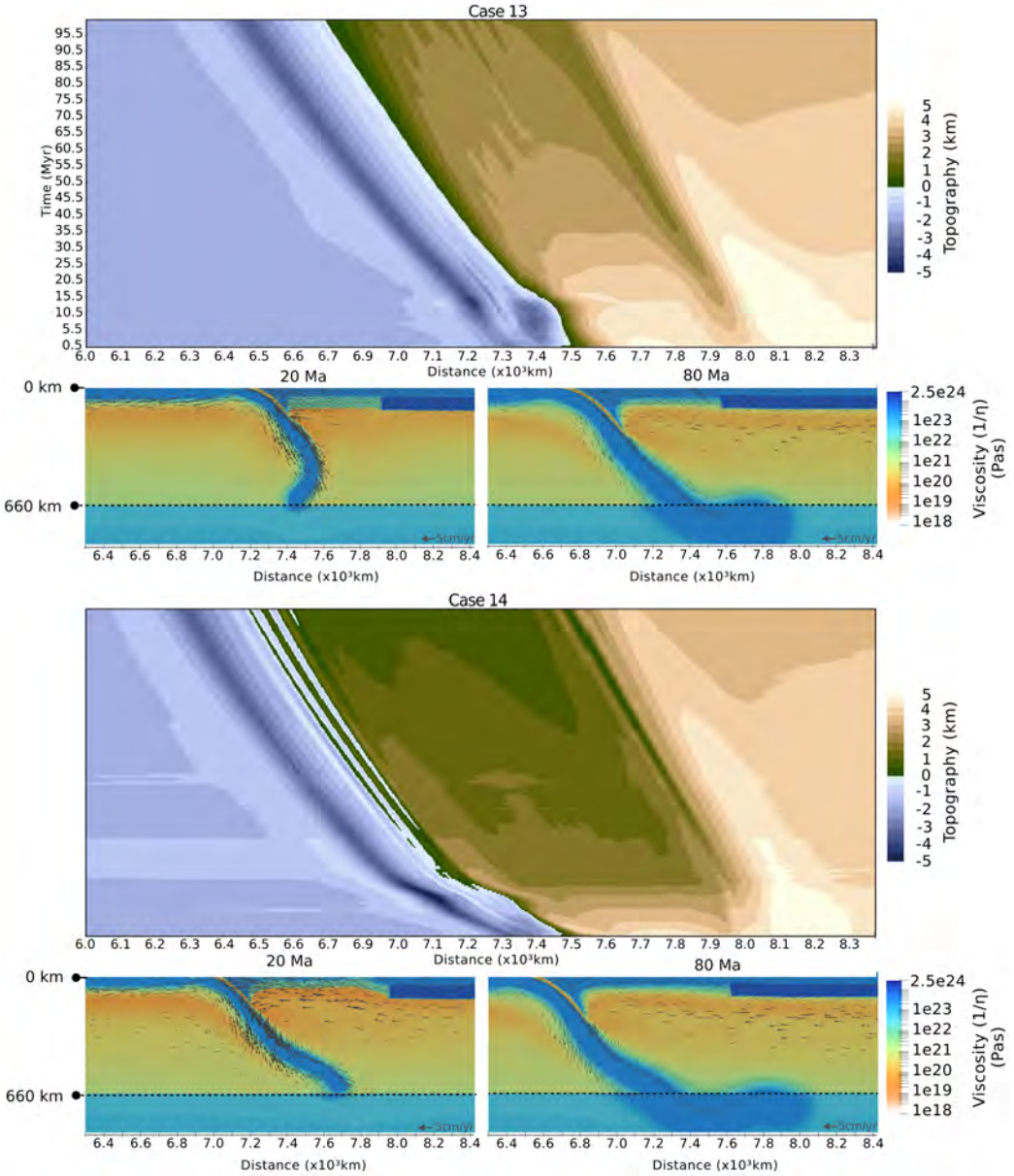

Figure 5: Effect of variations in margin deformation: case 13 (left) with reduced continental plastic yielding; case 14 (right) increased continental plastic yielding. Top row and bottom row same as Fig.3

with keel geometry variations tend to slightly favour increases in trench retreat over increases in the width of deformation area (Fig. 6). Models with keel rheology variations show slightly higher rates of increase in the width of the margin deformation over the amount of trench retreat.

Fig. 6 shows that the keel influence on the overriding plate can be grouped into three categories. Models with limited keel influence (group A - case 6) exhibit a restricted deformation extent with limited margin width, topography changes and no basin formation on the overriding plate. The models in group A have limited trench retreat, and a steep slab angle and morphology in the upper mantle (Table 2). Group C models (cases 7 and 10) show significant trench retreat (890 km and 710 km respectively) and extensive deformation widths (360 km and 440 km respectively) along the continental plate margin. In group C, slabs flatten and travel horizontally at 660 km depth until they avalanche into the lower mantle during the model later stages. These models exhibit multiple basin nucleation events and deep subsidence within the continental plate margin. Most models, however, sit between these two end members (Group B - cases 4, 5, 8, 9). The Group B models combine a modest continental plate margin deformation width (130 km, 125 km, 310 km, 320 km respectively) with modest to high trench rollback (860 km, 790 km, 760 km, 725 km respectively). These models undergo temporary slab anchoring at 660 km depth without the extensive flattening observed for Group C models. A central basin, flanked by two zones of higher topography, is also distinctive of group B models and is reminiscent of horst and graben struc-

tures observed in places like the Basin and Range along the North American margin (Table 2).

We observe a significant distinction between geometry and rheological effects (Fig. 7). Geometry variations (cases 11 and 12) result in a spatially limited deformation front (60 and 50 km respectively) and limited to modest trench retreat extents (755 and 580 km respectively). However, in the case of rheological heterogeneity (determined here by the amount of plastic yielding allowed in the model) there is a clear trend of increasing trench retreat with a widening of the deformation front on the overriding plate (Table 2), consistent with the keel variations models discussed above. Models with higher plastic yielding exhibit larger amounts of trench retreat and wider deformation fronts on the overriding plate than those with limited plastic yielding. Higher plastic yielding produces the highest amount of trench retreat (990 km) and the widest deformed overriding plate margin (430 km).

Excluding models with margin geometry variations, where the continental plate margin deformation is dominated by the spatial limits of the margin itself, the linear relationship exhibited in Figs. 6 and 7 indicates strong coupling between the subducting plate and the weaker, more mobile continental plate margin. This suggests that the overriding plate margin is being dragged and extended as the slab rollsback and the trench retreats. While it is clear that the subducting slab drives the dynamics of the system, the structure of the overriding plate controls how much of that driving force is partitioned between the slab rollback and the drag of the continent towards the trench.

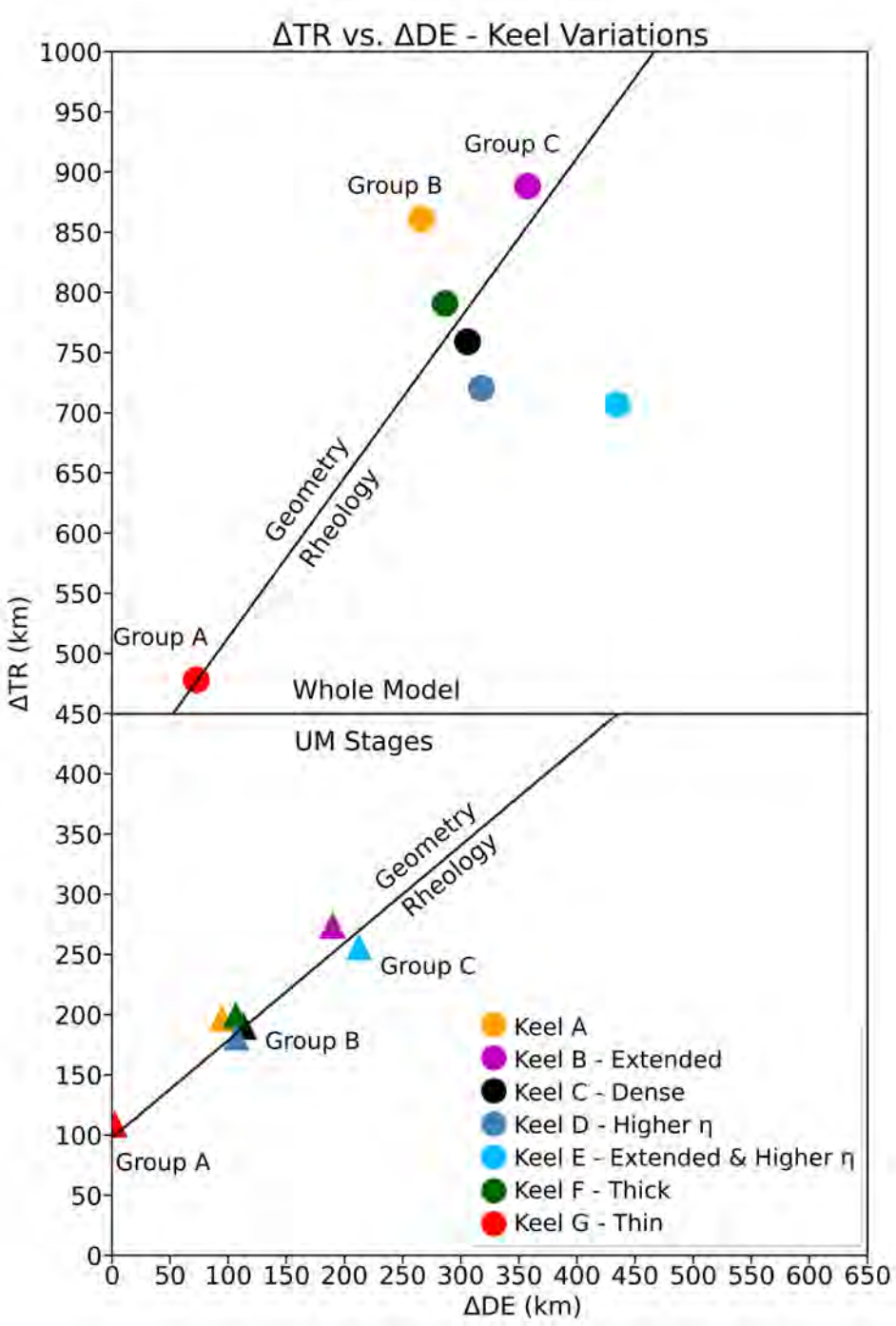

Figure 6: Trench retreat (ΔTR) vs. width of deformed continental plate margin area (ΔDE) for keel variations for the whole model (top) and upper mantle stages (bottom).

The continental structure also determines where the plate driving forces are partitioned on the overriding plate and spatially limits the extent of the subducting plate influence on the overriding plate, discussed next.

3.5. The role of continental heterogeneity on strain rates and velocity partitioning

In models with continental heterogeneity subducting plate velocity increases (ranging from 4.1 cm/yr... 3.5 cm/yr) concur with periods of high strain rates ($1 \cdot 10^{-15}$ ... $0.6 \cdot 10^{-15}$) within the continental plate margin; however, for homogeneous cases the opposite is true (Fig. A.16). The same trend also holds for convergence velocities for heterogeneous and homogeneous cases which suggest that that periods of higher strain rates should also correspond to higher continental plate velocities (Fig. A.17). This is true for the deformed, continental plate margin region; however, strain rates and the continental interior velocities are anti-correlated for keel cases, and in homogeneous cases, strain rates are correlated with continental interior velocities (Fig. 8).

This suggests that the subducting slab and continental plate margin are coupled, where both move in the same direction and follow similar trends in velocities (e.g. case 4 high subducting plate velocities of 4.1 cm/yr correspond to high margin velocities of 2.5 cm/yr, Figs. 5, 8). Deformation is controlled by the drag induced by the slab and the trench-ward mantle return flow it induces on one side, pulling the weaker margins towards the trench, and the

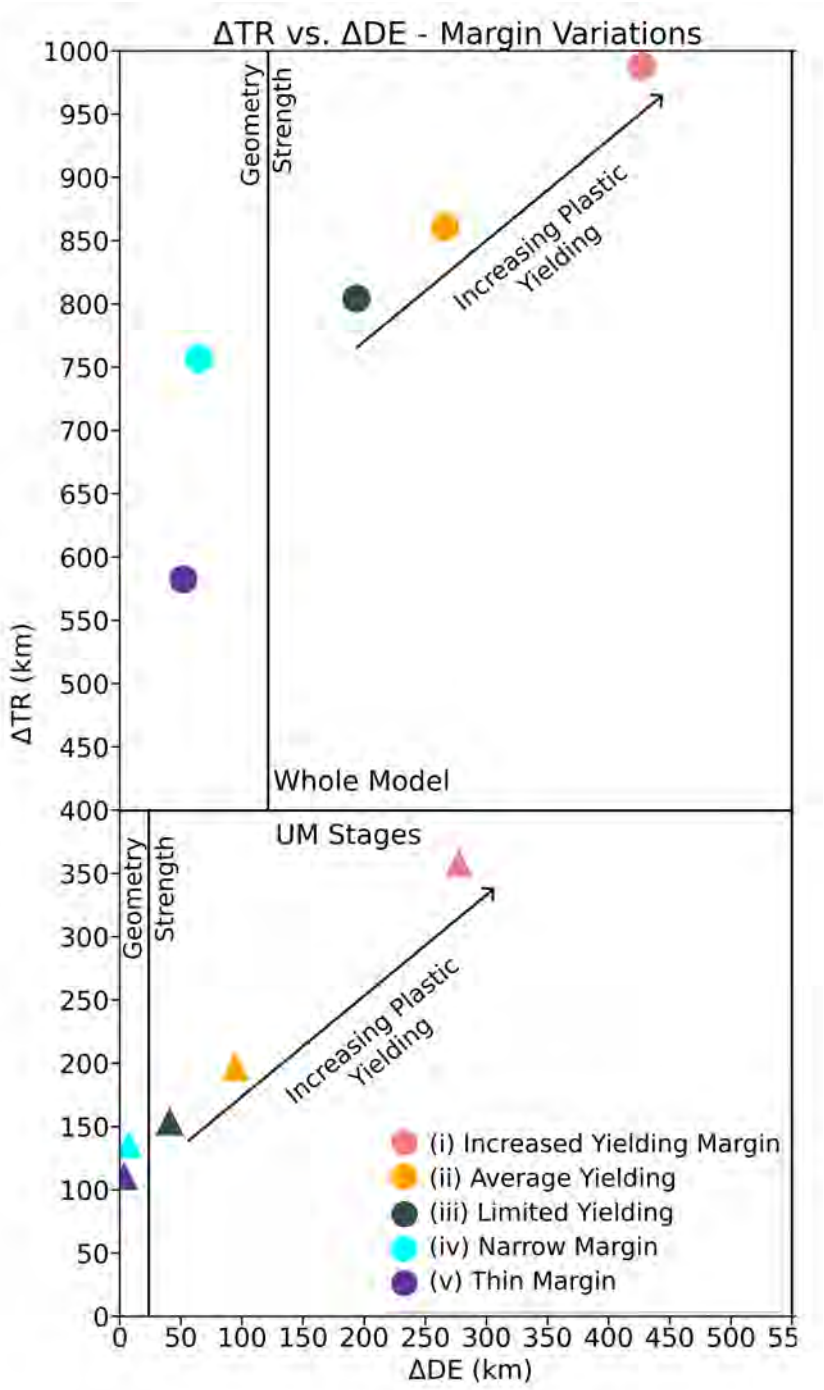

Figure 7: Trench retreat (ΔTR) vs. width of deformed area (ΔDE) along the continental plate margin for margin variations for the whole model (top) and upper mantle stages (bottom).

stabilising influence of the continental keel (Fig. A.14, A.15). This is true for all models with a continental keel but this effect is pronounced in keel-case 7 and margin-case 14 (Fig. 2). In the former, the extended nature of the keel results in a continental interior which is slower (0.3 cm/yr) than the margin (1.6 cm/yr), while in the latter, the weaker margin accumulates larger strain rates ($1 \cdot 10^{-15}$ s^{-1}) and higher velocities (2.5 cm/yr), while the continental interior maintains near constant strain rates of $0.1 \cdot 10^{-15}$ and velocities of 0.5 cm/yr (Figs. A.15, 8d, A.18d). These trends dominate during the model's first 15...20 Myrs and initiate the subsidence observed in the model topography.

Plate velocities are also correlated with the slab dynamics in the upper mantle. Fast convergence rates (e.g. cases 7 and 14, Fig. A.17a-b) are associated with slab flattening at 660 km depth. Slab flattening induces stronger return flow within the mantle wedge compared to other slab morphologies (Figs. A.14, A.15, 2.8 cm/yr for flat slab vs. 2.2 cm/yr for standard). The continental keel then forces this induced viscous flow within a narrow zone underlying the continental plate margin, exerting thus an additional drag on the continental plate margin in the direction of the return flow and towards the trench (cf. O'Driscoll et al., 2009).

Fig. A.14 illustrates how the velocity within the continental plate margin is split, with the faster trench-ward edge of the margin overlying the zone of faster channel return flow within mantle wedge. Fig. A.14 also shows that the differential velocities within the overriding plate correspond to a zone

In press at EPSL, June 2024.

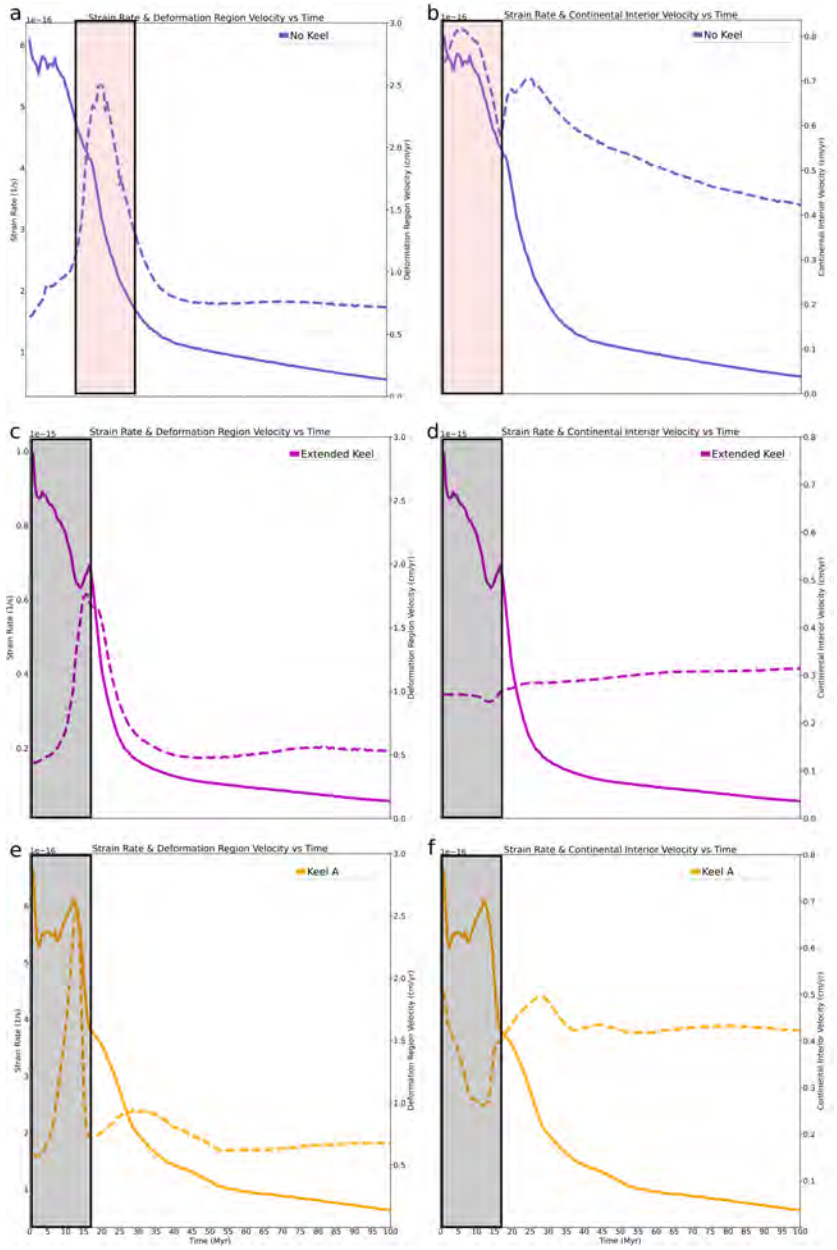

Figure 8: Left column: continental plate margin velocities, right column: continental interior velocities. Solid lines show strain rates and dashed lines show velocities. Top row: Case 2 (no keel), middle row: Case 7 (extended keel), bottom: Case 4 (standard keel) showing how for models with continental heterogeneity (keels) strain rates correlate with deformed continental plate margin velocities and are anti correlated with the continental interior velocities. The same trend is also observed for models with keels and variations in continental plate margin properties (Fig. A.18)

of localized strain-rates within the central axis of the margin. This strain focusing allows for the nucleation of subsidence within the margin into a central basin (Fig. A.15). At the surface this results in extensive trench retreat (e.g. 890 km and 990 km for cases 7 and 14 respectively, Table 2) and wide, extended back-arc basins (e.g. 360 km and 430 km for cases 7 and 14 respectively).

Models with thin keels and margins do not exhibit this relationship between the trench retreat and the continental plate margin extent. Fig. A.14c shows that velocity is uniform across the thin continental plate margin and the continental interior. The thin continental keel thus is ineffective at focusing the induced mantle flow (2.3 cm/yr) into a narrow high-velocity channel observed in the previous models and as a result there are no "pull-apart" forces acting on the margin, and therefore no extension and a sustained and defined basin presence. This indicates that the presence of a thick continental keel enhances and focuses the induced viscous flow in the mantle wedge into a high-velocity channel directly underlying the continental plate margin effectively dragging the continental plate margin towards the trench (cf. O'Driscoll et al., 2009; Paul et al., 2023). .

The continental properties thus determine how deformation is partitioned across the overriding plate. Focusing of higher strain rates ($10^{-15}\ldots10^{-16}\,\mathrm{s}^{-1}$) within the margin controls the width of the deformation area (increases in ΔDE are proportional to increases in strain rates, cf. Fig. A.19), weakening and extension experienced by the continental plate margin. This substan-

In press at EPSL, June 2024.

tiates the results of Wolf and Huismans (2019); we show that where plate velocities are partitioned determines the continental deformation and that continental keels play an important role in the weakening of the continental plate margin, and back-arc basin formation.

4. Discussion

4.1. Model limitations

Our models indicate that vertical and lateral rheological heterogeneity within the continental lithosphere modulates slab rollback, overriding plate deformation, back-arc basin formation, and so potentially continental extension.

In nature, the strength of the lithosphere is expected to be controlled by a range of factors, including lithological variations, evolving grain size, and other damage memory (e.g. Hirth and Kohlstedt, 2004; Montési, 2013; Bercovici and Ricard, 2016). Such effects are only approximately represented by our relatively simple rheological setup. In particular, we do not account for a reduction in plastic yield stress with progressive deformation and thus have no strain localisation. Were we to include localization, we would expect the difference in topography formation scenarios to be even more pronounced.

The rheology of our models is also simplified by excluding a multi-mineralic slab and mantle, and ignores the effects of phase changes. Moreover, mantle flow in nature is, of course, 3-D, a possibly more restrictive simplification. Work by Manea et al. (2012) and Taramón et al. (2015) shows that for 3-D

flat subduction the cratonic lithosphere is strongly coupled to the subducting slab, enhancing further the upwards suction of the slab and closure of the mantle wedge. This supports our 2-D results and suggests that in 3-D continental heterogeneity effects might be comparable, or perhaps locally even more pronounced.

While slab dynamics, including the temporal evolution of trench retreat, and the partitioning of the plate velocities may thus be affected by all of these complexities, we expect the relative effects of keels on deformation to be fairly similar.

4.2. Analogues in nature

Our models are not designed for specific subduction zones; instead, we seek to investigate how continental heterogeneity impacts the dynamics and overriding plate deformation, in general. Therefore, we can only make broad comparisons between models and real world examples.

In terms of overall kinematics of plate velocities (e.g. Sdrolias and Müller, 2006; Capitanio et al., 2010; Faccenna et al., 2014), during major deformation events, narrow margins such as Ryukyu exhibit similar overriding and subducting plate velocities. Such deformation behavior is found for our case 12 during the basin formation event, although the absolute velocities are higher than for the natural case. More generally, the timing of deformation and basin formation in nature is typically ~ 10 Myr (Sdrolias and Müller, 2006), which is similar to the ~ 15 Myr period of high strain rates and deformation

our models.

We find that a combination of weak continental plate margins and strong, extended keels favour wide zones of deformation (360-430 km) and extensive subsidence (3.5 km). These margins exhibit multiple basins and significant asymmetry reflecting the partitioning of the asthenospheric drag underneath the continental plate margin. Models with wide zones of back-arc deformation record the highest amount of trench rollback (890-990 km). This behaviour is consistent with the highly extended, asymmetric back-arc deformation observed in, e.g., the Pannonian and Aegean basins (Wortel and Spakman, 2000; Faccenna et al., 2014) which also record multiple basins and considerable subsidence (1-4 km; Meulenkamp et al., 1996; Horváth et al., 2015). Trench rollback for the Pannonian basin is estimated to be ~ 450 km and the amount of extensional deformation for the Aegean basin is $\sim 400 \ldots 500$ km with some remaining debate (e.g. Faccenna et al., 2014). This is broadly consistent with Mediterranean back-arcs being affected by a mix of rheologically variable lithosphere, contributing to the rollback driven extension of the continental plate margin.

The properties of the continental keel can also contribute to the uplift of the continental plate margin. In case 8 (Fig. 6), a denser than reference keel produces a neutrally buoyant continental lithosphere and an isostatically uplifted continental plate margin. The overall uplift signal is recorded within a relatively narrow back-arc region similar to that of cases 4, 5, and 9 (Fig. 6). The uplifted margin in case 8 also records a central, and nar-

row basin suggesting an analogy to the Andean intermontane basins (e.g. Horton, 2005). Although the latter are significantly shallower than the central basin in case 8 (0.8 km vs. 3 km), they both show similar structural features, i.e., both basins occur within elevated domains, for case 8 this is the isostatically elevated margin (5 km high elevations) and in the Andean intermontane basins case, this is the $\sim$ 4 km high central Eastern Cordillera (Horton, 2005).

Similar aspects of the tectonics can also be found within the late Cretaceous to early Paleogene intermontane basins of the Laramide in the Basin and Range area, and around the Colorado Plateau (e.g. Lawton, 2019). In this case, the continental lithosphere was likely strongly modified by the flat slab episode, leading to hydration and/or removal of mantle lithosphere and hence lateral viscosity contrasts similar to our models, although the gravitational potential energy distributions and overall setting are different from our simple subduction models.

Comparing kinematics for the Andean subduction case, fast subducting slab and slow overriding plate velocities are found during periods of basin formation (Sdrolias and Müller, 2006; Capitanio et al., 2010), and we observe a similar but more subdued trend for case 8 during its period of high strain rates and basin formation.

5. Conclusions

The structure of the overriding continental plate directly influences the evolution of topography and deformation within the continental plate margin. Variations in keel and margin properties also modulate the slab behaviour, the amount of trench retreat, and the partitioning of the slab-induced flow across the continental plate margin and between the margin and the continental interior.

Wide zones of deformation and extensive subsidence form within the back-arc region when the continental keel is strong and extended, and the margins are weak. Thin, spatially limited keels, and strong margins produce narrow back-arc margins. In nature, back-arc extension and subsidence may thus not only reflect convergence kinematics and local structure, but may also be affected by the adjacent continental lithosphere.

Large extended back-arc regions such as the Pannonian and the Aegean back-arcs may be a result of an interplay between fast slab rollback and a weak continental plate margin combined with a strong and wide continental keel. Narrow margins such as the Okinawa trough in NE Japan may be indicative of a comparatively stronger continental plate margin and weaker and/or smaller continental keel. Continental keel properties can also influence the uplift of the deformation front and encourage the formation of intermontane basins in regions such as the Andes and within the Laramide orogeny.

Our study underscores the importance of considering heterogeneities in

In press at EPSL, June 2024.

the continental lithosphere, such as keel and margin properties, when investigating subduction zone dynamics. Further, integrative modeling adapted to real-world subduction systems should contribute to a more comprehensive understanding of the complex interactions between oceanic plate subduction and the highly variable continental lithosphere.

Acknowledgments

TWB was partially supported by NSF EAR 1925939 and 2045292, and computations were performed on the NSF supercomputer *Frontera* at the Texas Advanced Computing Center. We thank the developers and Computational Infrastructure for Geodynamics (geodynamics.org) which is funded by the National Science Foundation under award EAR-0949446 and EAR-1550901 for supporting the development of ASPECT.

Appendix A. Appendix

Appendix A.1. The top boundary condition question - free slip or free surface?

We explore the influence of a free surface and free slip top boundary condition on the evolution of topopgraphy, continental extension, trench retreat, and slab behaviour for cases 1-4 (Table A.4). For keel-free-case 1, there is little variation between the free surface and the free slip implementations for the slab morphology both at 20 Myrs when the slab is in the upper mantle, and also at 80 Myrs when the slab has sunk into the lower mantle. Strain rates are also similar and the topography at the surface is comparable save for minor, small-scale features (Fig. A.9). For reference-keel-case 2 we maintain a similar continental lithosphere thickness but introduce a 75 km thick, higher viscosity continental keel (Table A.4) at the bottom of the continental lithosphere. We find that similar to test case 1, in test case 2 there is very little variation in the slab morphology, strain rates, or topography recorded throughout the model evolution for both the free surface and the free slip cases.

Next, in keel-free-case 3, we further explore the effects of vertical viscosity variations by introducing a viscosity reduction of an order of magnitude within the bottom 50 km of the continental lithosphere (Table A.4 and sec. 2.3). We find that for these models the nature of the top boundary condition of the model is important and can result in significant differences in strain rates and in the evolution of the continental topography for the free

In press at EPSL, June 2024.

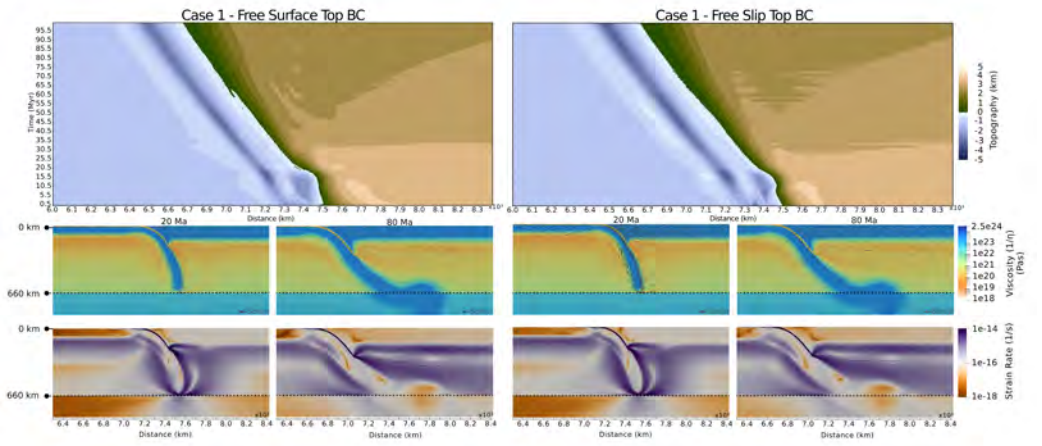

Figure A.9: Surface boundary conditions for keel-free-case 1 models with initial homogeneous continental η implementation. Left: Free surface boundary condition. Right: Free slip boundary condition. Top row: Topography; middle row: viscosity and induced viscous flow velocity; bottom row: strain rates

surface and free slip versions Fig. A.13. Fig. A.11 clearly shows that for test case 3 the free surface implementation exhibits significant focusing of higher strain rates within the continental lithosphere for the first 30 Myrs of model evolution. This produces significant topographic contrast with multiple horst and graben-like features on the overriding plate which eventually coalesce into broader wavelength zones of higher and lower topography. These variations in topography and strain rates within the overriding plate are missing in the same model set-up with a free slip top boundary condition (Fig. A.11). However, slab behaviour across the two set-ups is similar.

In keel-case 4 we include a continental keel similar to that of case 2 and maintain a viscosity reduction similar to case 3 but limit this to the keel-free margin of the continental lithosphere (secs. A.4 and 2.3). Comparing the free

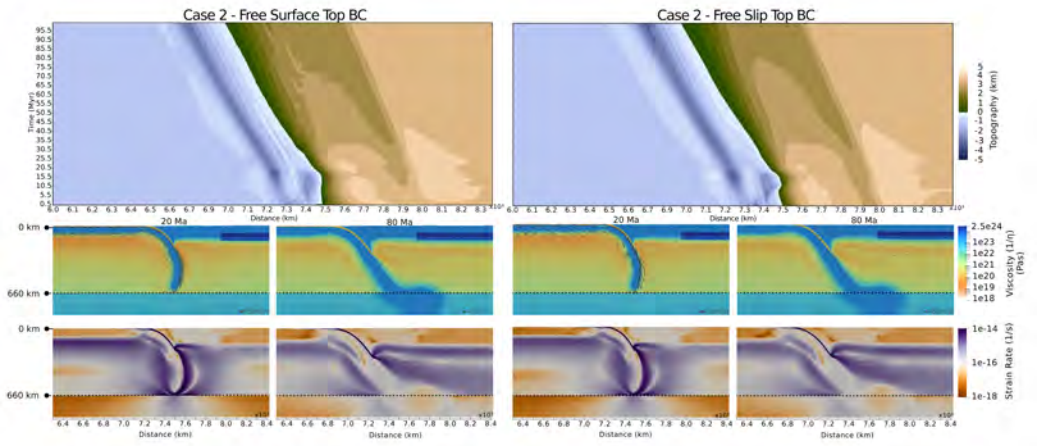

Figure A.10: Surface boundary conditions for reference-keel-case 2 models with initial homogeneous continental η and continental keel implementation. Left: Free surface boundary condition. Right: Free slip boundary condition. Top row: Topography; middle row: viscosity and induced viscous flow velocity; bottom row: strain rates

surface and free slip versions of test case 4 we find that similar to test case 3 the nature of the top boundary condition plays a significant role in both the strain rates and their focusing, as well as the evolution of topography at the surface. Here too, we observe strain rate focusing within the keel-free ∼200 km continental plate margin, leading to the development of a well-defined central basin bounded by two areas of higher topography on either side. This topographic signal is maintained through the model evolution, even as the continental overriding plate undergoes overall subsidence. The free slip version of this set-up is missing both the focusing of the higher strain rates within the continental plate margin (i.e. the keel-free space between the continental edge and the keel edge) and the formation of a central basin bounded by two shoulders of higher topography (Figs. A.12 and A.13).

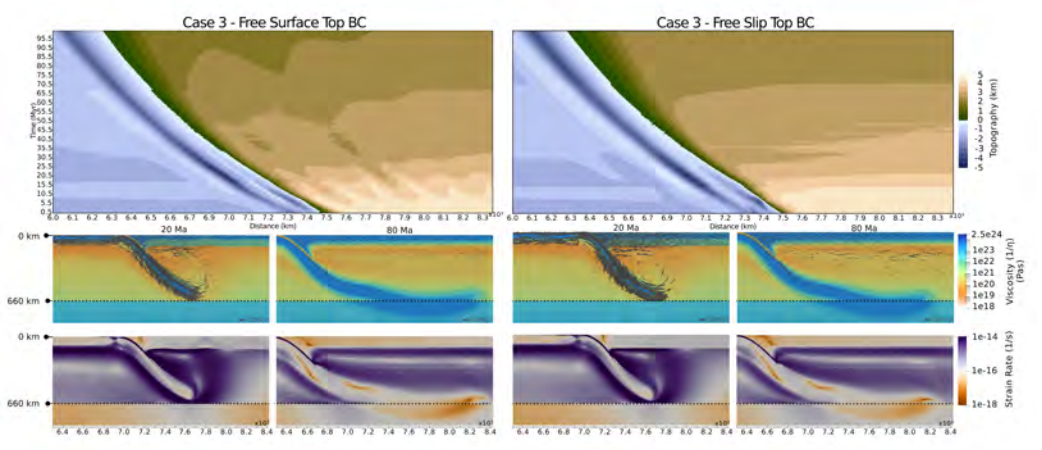

Figure A.11: Surface boundary conditions for keel-free-case 3 models with continental η variations. Left: Free surface boundary condition. Right: Free slip boundary condition. Top row: Topography; middle row: viscosity and induced viscous flow velocity; bottom row: strain rates

Similar to test cases 1-3, slab morphology in test case 4 does not seem to be impacted by the type of the top boundary condition implemented.

Appendix A.2. Margin and keel properties

For this study we first test the impact of top boundary conditions on the evolution of topography and slab dynamics in cases 1-4. We then analyze the role of variations in continental keel properties (cases 4-10) and continental plate margin properties (cases 11 -14). The variations tested are detailed in Table A.4. Continental heterogeneity has a first-order impact on the margin subsidence and extent, the number of basins within the back-arc region, the elevation change within the continental interior, the trench depth, and the trench rollback described in Table 2 for each model tested.

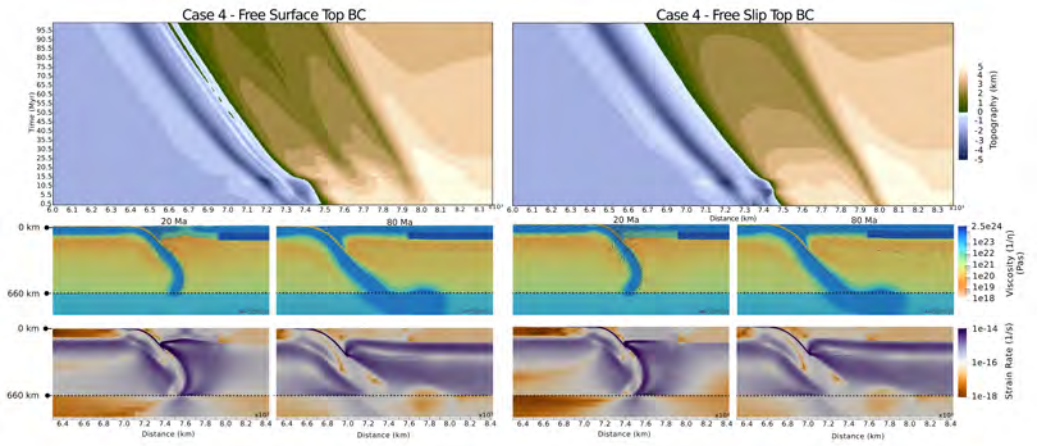

Figure A.12: Surface boundary conditions for keel-case 4 models with continental η variations and keel implementation. Left: Free surface boundary condition. Right: Free slip boundary condition. Top row: Topography; middle row: viscosity and induced viscous flow velocity; bottom row: strain rates

Model	Margin Subsidence (km)	Margin Extent (km)	Number of Margin Basins	Interior Elevation Change (km)	Trench Depth (km)	Trench Rollback (km)	Slab Angle* Whole Model (∘)	Slab Angle Upper Mantle (∘)	Strain Rates Whole Model (s^{-1})	Strain Rates Upper Mantle (s^{-1})
Case 1^a	2.5	N/A	N/A	2.5	2.75	85	55.2	74.8	$1.0 \cdot 10^{-16}$	$2.3 \cdot 10^{-16}$
Case 1^b	2.5	N/A	N/A	2.5	2.75	85	66.6	79.1	$1.5 \cdot 10^{-16}$	$2.0 \cdot 10^{-16}$
Case 2^a	1	94	1	1	3.5	60	59.3	79.6	$1.2 \cdot 10^{-16}$	$2.5 \cdot 10^{-16}$
Case 2^b	1	80	1	1	3.25	60	59.3	79.6	$1.1 \cdot 10^{-16}$	$2.1 \cdot 10^{-16}$
Case 3^a	3.5	47	1	3	4	124	46.6	65.5	$1.9 \cdot 10^{-16}$	$5.3 \cdot 10^{-16}$
Case 3^b	3	N/A	N/A	3	4.5	122	49.7	70.2	$1.8 \cdot 10^{-16}$	$4.3 \cdot 10^{-16}$
Case 4	3	130	1	1.5	4	860	54.9	73.5	$2.1 \cdot 10^{-16}$	$5.4 \cdot 10^{-16}$
Case 4^b	2.75	92	N/A	1.25	4.75	850	74.2	74.2	$2.5 \cdot 10^{-16}$	$2.5 \cdot 10^{-16}$

Table A.3: Same as Table 2 but subduction parameters are now measured for models with keel variations (cases 2 and 4) with a free surface (^{a}) and a free slip (^{b}) implementations. Note: Cases 1^a-^{b} and 3^b do not have a defined continental plate margin. In these cases the subsidence and interior elevation changes record the elevation changes which occur over the continental overriding plate as a whole.

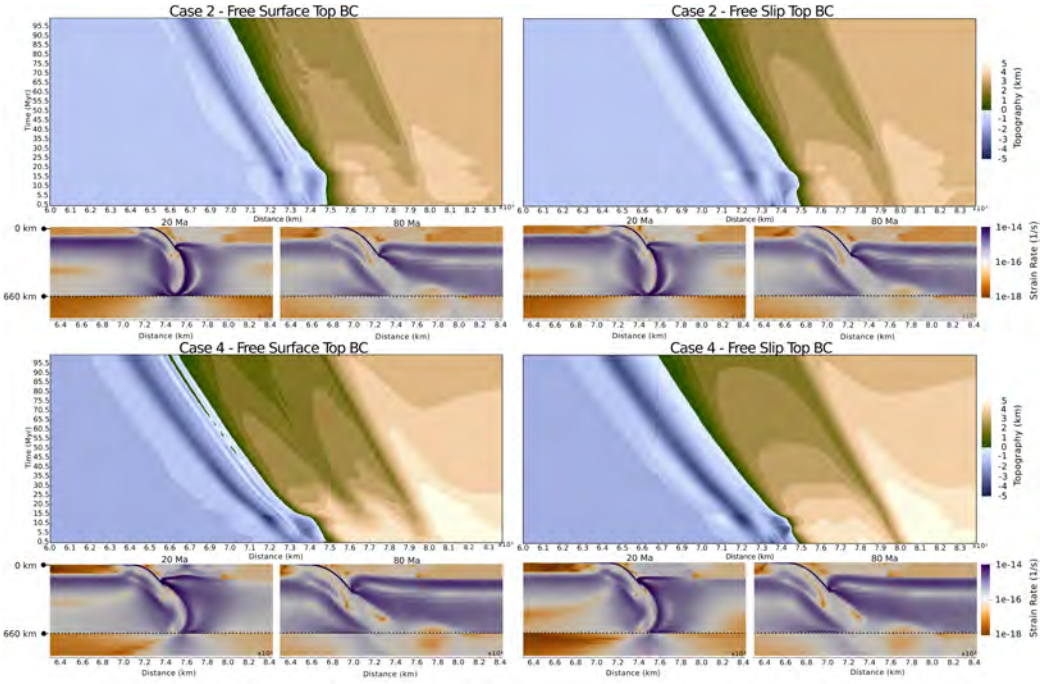

Figure A.13: Surface boundary conditions tests. Top six panels show results form reference-keel case 2 with homogeneous continental η and continental keel implementation. Left: Free surface boundary condition. Right: Free slip boundary condition. Top row: Topography as a function of horizontal distance and time; bottom row: strain rates and slab configuration for two timesteps. Bottom six panels show the same fields for keel case 4 with continental η variations and keel implementation.

Model	Lower OP η (Pa s)	Lower OP T (K)	Keel Thickness (km)	Keel Length (km)	Keel η (Pa s)	Keel ρ (kg m^{-3})	Margin Thickness (km)	Margin Extent (km)	λ
Case 1	$2.5 \cdot 10^{23}$	500	N/A	N/A	N/A	N/A	N/A	N/A	N/A
Case 2	$2.5 \cdot 10^{23}$	500	75	200	$2.5 \cdot 10^{24}$	3150	150	200	0.5
Case 3	$2.5 \cdot 10^{21}$	1573	N/A	N/A	N/A	N/A	N/A	N/A	N/A
Case 4	$2.5 \cdot 10^{21}$	1573	75	200	$2.5 \cdot 10^{24}$	3150	150	200	0.5
Case 5	$2.5 \cdot 10^{21}$	1573	100	200	$2.5 \cdot 10^{24}$	3150	150	200	0.5
Case 6	$2.5 \cdot 10^{21}$	1573	50	200	$2.5 \cdot 10^{24}$	3150	150	200	0.5
Case 7	$2.5 \cdot 10^{21}$	1573	75	900	$2.5 \cdot 10^{24}$	3150	150	200	0.5
Case 8	$2.5 \cdot 10^{21}$	1573	75	200	$2.5 \cdot 10^{24}$	3330	150	200	0.5
Case 9	$2.5 \cdot 10^{21}$	1573	75	200	$2.5 \cdot 10^{26}$	3150	150	200	0.5
Case 10	$2.5 \cdot 10^{21}$	1573	75	900	$2.5 \cdot 10^{26}$	3150	150	200	0.5
Case 11	$2.5 \cdot 10^{21}$	1573	75	200	$2.5 \cdot 10^{24}$	3150	150	150	0.5
Case 12	$2.5 \cdot 10^{21}$	1573	50	200	$2.5 \cdot 10^{24}$	3150	100	200	0.5
Case 13	$2.5 \cdot 10^{21}$	1573	75	200	$2.5 \cdot 10^{24}$	3150	150	200	0.3
Case 14	$2.5 \cdot 10^{21}$	1573	75	200	$2.5 \cdot 10^{24}$	3150	150	200	0.07

Table A.4: Keel and margin variations for models with a free surface and a free slip top boundary condition, where OP is the overriding plate

Appendix A.3. Partitioning of plate velocities and strain rates

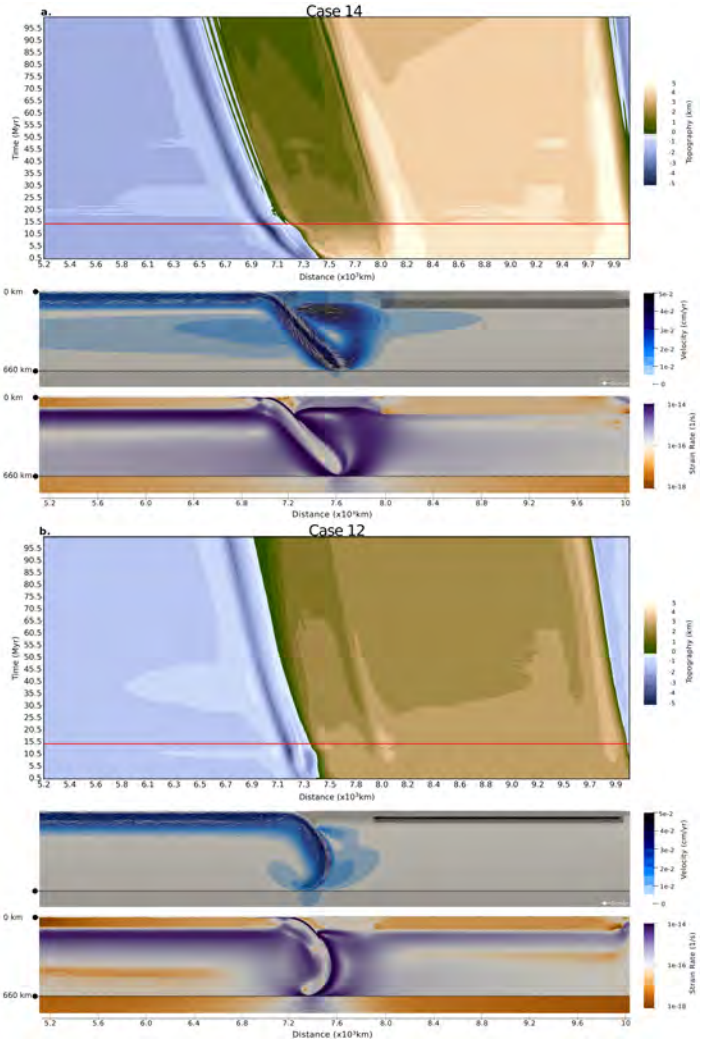

Figure A.14: Top row: free surface topography, middle row: plots of the velocity magnitude, bottom row: strain rate plots for case 14 (weaker margin) and case 12 (thin margin and keel), showing how the properties of the continent influences the presence of channeled flow beneath the margin, leading to a partitioning of velocities across the margin and keel and ultimately focusing of strain-rates and deformation within the continental plate margin.

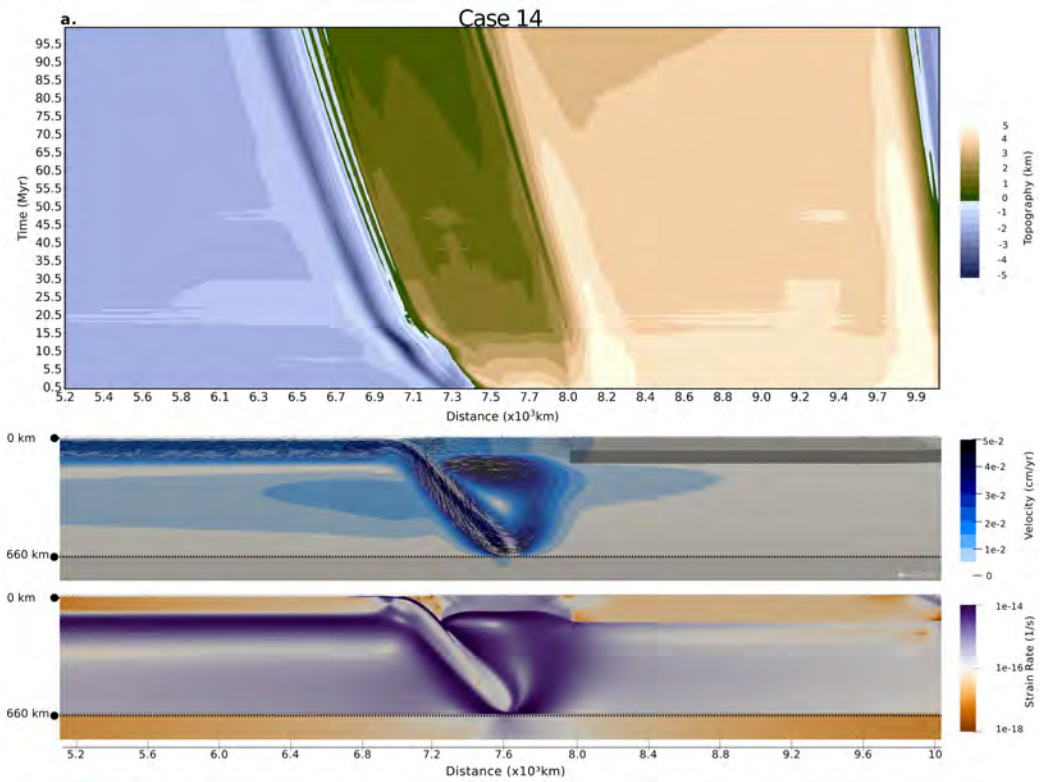

Figure A.15: Zoomed in view for Fig. A.14 showing the free surface topography, the velocity magnitude and strain rate for case 14 (weaker margin). Note the strain-focusing patterns following the velocity partitioning within the continental plate margin and the shear bands linking the central subsidence with the margin shoulders

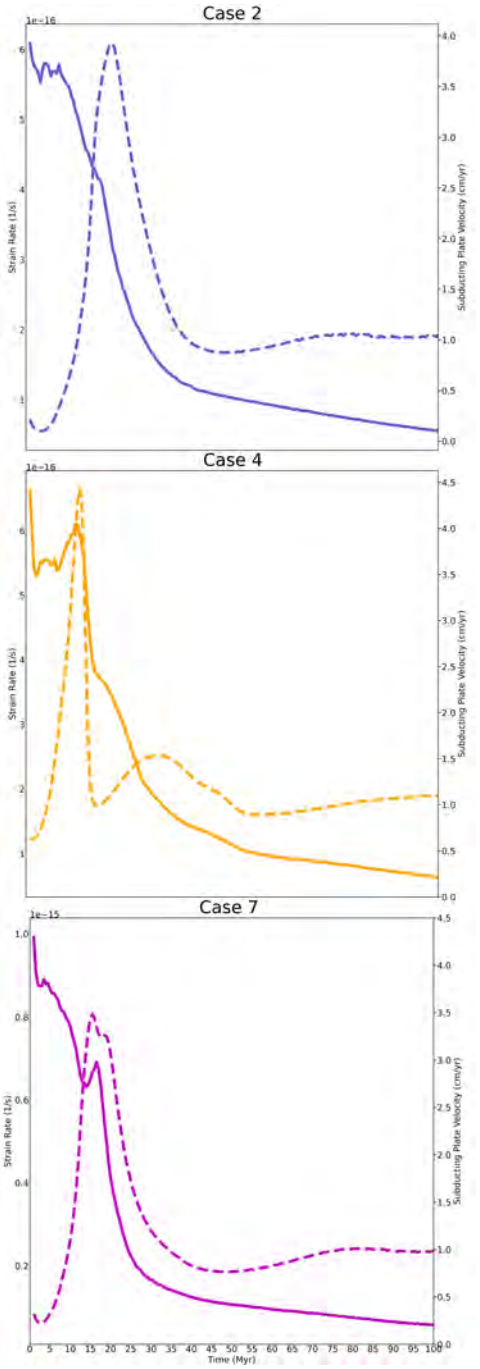

Figure A.16: Solid Lines: strain rates, dashed lines: subducting plate velocities against time for case 3, case 4 and case 7, showing how for keel cases subducting plate velocity increases are concurrent with periods of high strain.

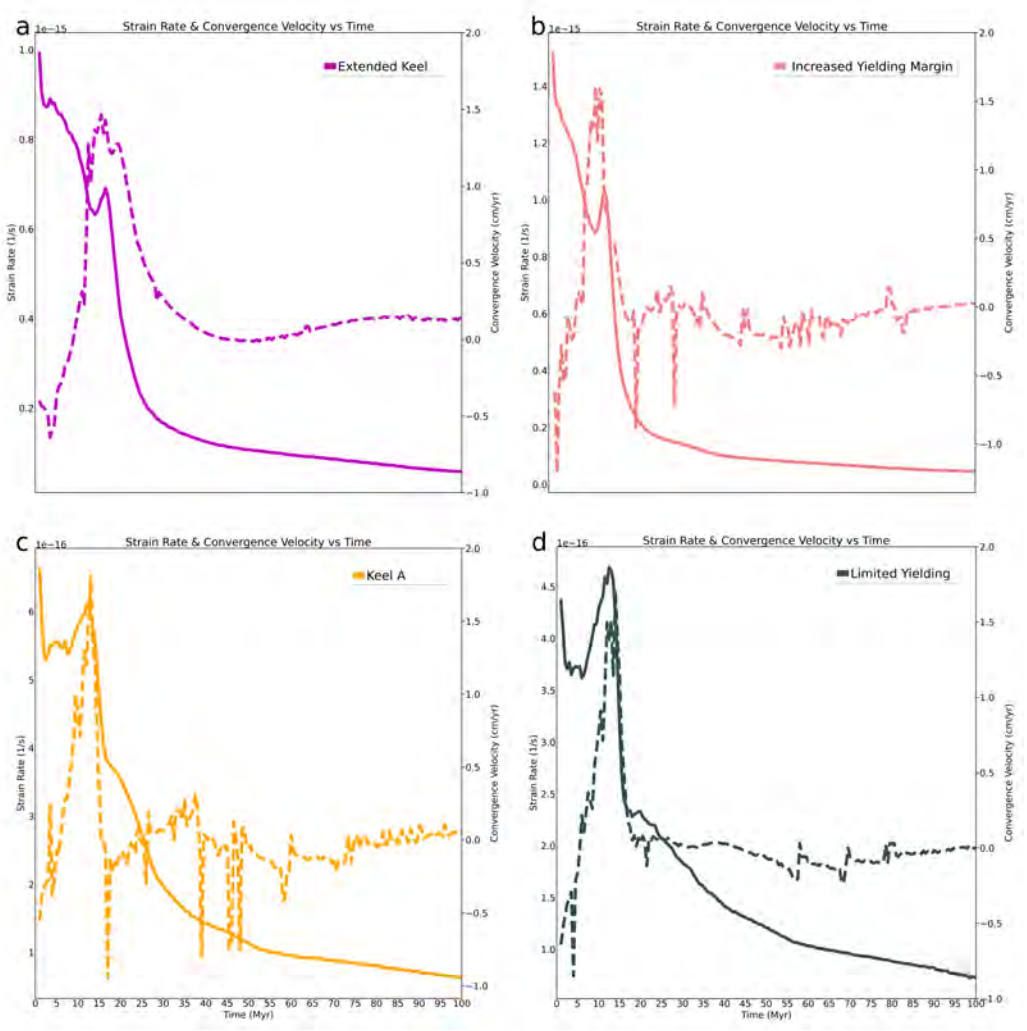

Figure A.17: Solid Lines: strain rates, dashed lines: convergence plate velocities against time for cases 7 and 14 (top) and cases 4 and 13 (bottom) illustrating the correlation between high convergence rates and strain rates. Note that models with extreme subsidence and wide continental margin deformation area exhibit lower convergence velocities compared to case 4 and case 13.

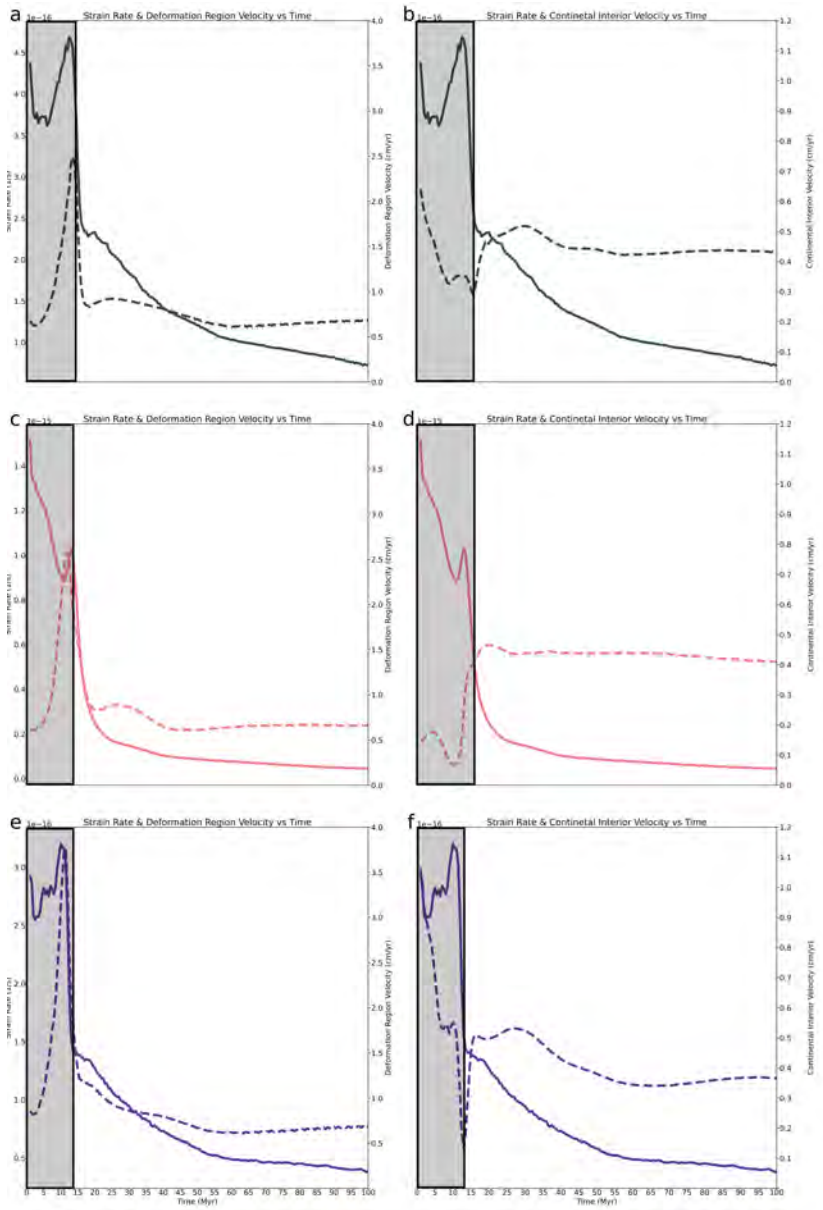

Figure A.18: Left column continental plate margin velocities, right column continental interior velocities for continental plate margin variations. Solid lines show strain rates and dashed lines show velocities. Top row: Case 13 (strong margin), middle row: Case 14 (weak margin), bottom: Case 12 (thin continent) showing how strain rates correlate with deformed continental plate margin velocities and are anti correlated with the continental interior velocities.

Appendix A.4. Strain Rates and Area of Deformation on Continental Plate Margin

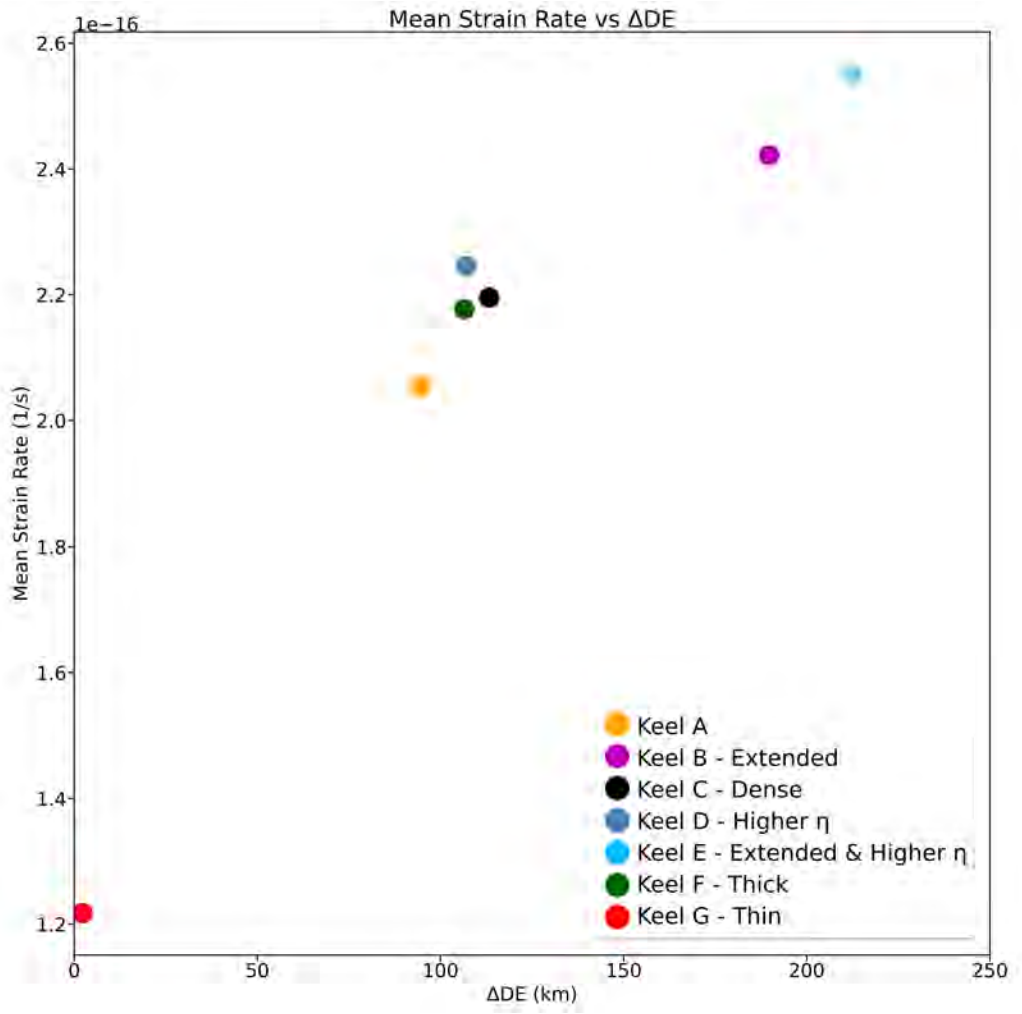

Figure A.19: Plot of continental margin strain rates against the area of continental margin deformation for models with keel property variations showing a linear relationship between increasing strain rates and wider are of deformation on the continental plate margin

References

Audet, P., Bürgmann, R., 2011. Dominant role of tectonic inheritance in supercontinent cycles. Nature Geosc. 4, 184–187.

Balázs, A., Burov, E., Matenco, L., Vogt, K., Francois, T., Cloetingh, S., 2017. Symmetry during the syn- and post-rift evolution of extensional back-arc basins: The role of inherited orogenic structures. Earth and Planetary Science Letters 462, 86–98. doi:10.1016/j.epsl.2017.01.015.

Bangerth, W., Dannberg, J., Fraters, M., Gassmoeller, R., Glerum, A., Heister, T., Naliboff, J., 2021. Aspect v2.3.0. URL: `https://doi.org/10.5281/zenodo.5131909`, doi:10.5281/zenodo.5131909.

Becker, T.W., 2006. On the effect of temperature and strain-rate dependent viscosity on global mantle flow, net rotation, and plate-driving forces. Geophys. J. Int. 167, 943–957. doi:10.1111/j.1365-246X.2006.03172.x.

Behr, W.M., Holt, A.F., Becker, T.W., Faccenna, C., 2022. The effects of plate interface rheology on subduction kinematics and dynamics. Geophys. J. Int. 230, 796–812. doi:10.1093/gji/ggac075.

Bercovici, D., Ricard, Y., 2016. Grain-damage hysteresis and plate tectonic states. Phys. Earth Planet. Int. 253, 31–47.

Billen, M.I., Hirth, G., 2005. Newtonian versus non-Newtonian upper mantle viscosity: Implications for subduction initiation. Geophys. Res. Lett.

32, n/a–n/a. URL: http://doi.wiley.com/10.1029/2005GL023457, doi:10.1029/2005GL023457.

Butterworth, N.P., Quevedo, L., Morra, G., Müller, R.D., 2012. Influence of overriding plate geometry and rheology on subduction. Geochemistry, Geophysics, Geosystems 13, n/a–n/a. URL: http://doi.wiley.com/10.1029/2011GC003968, doi:10.1029/2011GC003968.

Capitanio, F.A., Stegman, D.R., Moresi, L., Sharples, W., 2010. Upper plate controls on deep subduction, trench migrations and deformations at convergent margins. Tectonophys. 483, 80–92.

Chase, C.G., 1978. Extension behind island arcs and motions relative to hot spots. Journal of Geophysical Research 83, 5385. doi:10.1029/jb083ib11p05385.

Conrad, C.P., Lithgow-Bertelloni, C., 2006. Influence of continental roots and asthenosphere on plate-mantle coupling. Geophysical Research Letters 33, L05312. URL: http://doi.wiley.com/10.1029/2005GL025621, doi:10.1029/2005GL025621.

Crameri, F., Lithgow-Bertelloni, C., 2018. Abrupt upper-plate tilting during slab-transition-zone collision. Tectonophysics 746, 199–211. URL: https://doi.org/10.1016/j.tecto.2017.09.013, doi:10.1016/j.tecto.2017.09.013.

Dasgupta, R., Mandal, N., Lee, C., 2021. Controls of subducting slab dip and age on the extensional versus compressional deformation in the overriding plate. Tectonophysics 801, 228716. URL: https://doi.org/10.1016/j.tecto.2020.228716, doi:10.1016/j.tecto.2020.228716.

Enns, A., Becker, T.W., Schmeling, H., 2005. The dynamics of subduction and trench migration for viscosity stratification. Geophys. J. Int. 160, 761–775.

Erdős, Z., Huismans, R.S., Faccenna, C., 2022. Wide versus narrow back-arc rifting: Control of subduction velocity and convective back-arc thinning. Tectonics 41. doi:10.1029/2021TC007086.

Faccenna, C., Becker, T.W., Auer, L., Billi, A., Boschi, L., Brun, J.P., Capitanio, F.A., Funiciello, F., Horvàth, F., Jolivet, L., Piromallo, C., Royden, L., Rossetti, F., Serpelloni, E., 2014. Mantle dynamics in the Mediterranean. Rev. Geophys. 52, 283–332. URL: http://doi.wiley.com/10.1002/2013RG000444, doi:10.1002/2013RG000444.

Garel, F., Goes, S., Davies, D.R., Davies, J.H., Kramer, S.C., Wilson, C.R., 2014. Interaction of subducted slabs with the mantle transition-zone: A regime diagram from 2-D thermo-mechanical models with a mobile trench and an overriding

plate. Geochemistry, Geophys. Geosystems 15, 1739–1765. URL: https://onlinelibrary.wiley.com/doi/10.1002/2014GC005257, doi:10.1002/2014GC005257.

Ghosh, A., Becker, T.W., Zhong, S.J., 2010. Effects of lateral viscosity variations on the geoid. Geophysical Research Letters 37. doi:10.1029/2009GL040426.

Ghosh, A., Holt, W., Wen, L., 2013. Predicting the lithospheric stress field and plate motions by joint modeling of lithosphere and mantle dynamics. Journal of Geophysical Research: Solid Earth 118, 346–368.

Gordon, R.G., 2000. Diffuse oceanic plate boundaries: Strain rates, vertically averaged rheology, and comparisons with narrow plate boundaries and stable plate interiors, in: Richards, M.A., Gordon, R.G., van der Hilst, R.D. (Eds.), The History and Dynamics of Global Plate Motion. American Geophysical Union, Washington DC. volume 121 of *Geoophys. Mono.*, pp. 143–159.

Hager, B.H., 1984. Constraints on Mantle Rheology and Flow Residual Geoid: degree 2-10. J. Geophys. Res. 89, 6003–6015.

Heister, T., Dannberg, J., Gassmöller, R., Bangerth, W., 2017. High accuracy mantle convection simulation through modern numerical methods. II: Realistic models and problems. Geophysical Journal Inter-

national 210, 833–851. URL: https://doi.org/10.1093/gji/ggx195, doi:10.1093/gji/ggx195.

Heuret, A., Funiciello, F., Faccenna, C., Lallemand, S., 2007. Plate kinematics, slab shape and back-arc stress: A comparison between laboratory models and current subduction zones. Earth Planet. Sci. Lett. 256, 473–483. doi:10.1016/j.epsl.2007.02.004.

Heuret, A., Lallemand, S., 2005. Plate motions, slab dynamics and back-arc deformation. Physics of the Earth and Planetary Interiors 149, 31–51. URL: https://linkinghub.elsevier.com/retrieve/pii/S0031920104003462, doi:10.1016/j.pepi.2004.08.022.

Hirth, G., Kohlstedt, D., 2004. Rheology of the upper mantle and the mantle wedge: A view from the experimentalists. Geophys. Monogr. Ser. 138, 83–105. doi:10.1029/138GM06.

Holt, A.F., Becker, T.W., Buffett, B.A., 2015a. Trench migration and overriding plate stress in dynamic subduction models. Geophysical Journal International 201, 172–192. doi:10.1093/gji/ggv011.

Holt, A.F., Buffett, B.A., Becker, T.W., 2015b. Overriding plate thickness control on subducting plate curvature. Geophysical Research Letters 42, 3802–3810. doi:10.1002/2015GL063834.

Holt, A.F., Condit, C.B., 2021. Slab Temperature Evolution Over the Lifetime of a Subduction Zone. Geochemistry, Geophys. Geosystems 22. doi:10.1029/2020GC009476.

Horton, B.K., 2005. Revised deformation history of the central andes: Inferences from cenozoic foredeep and intermontane basins of the eastern cordillera, bolivia. doi:10.1029/2003TC001619.

Horváth, F., Musitz, B., Balázs, A., Végh, A., Uhrin, A., Nádor, A., Koroknai, B., Pap, N., Tóth, T., Wórum, G., 2015. Evolution of the Pannonian basin and its geothermal resources. Geothermics 53, 328–352. URL: http://dx.doi.org/10.1016/j.geothermics.2014.07.009, doi:10.1016/j.geothermics.2014.07.009.

Jordan, T., 1981. Continents as a chemical boundary layer. Phil. Trans. Royal Soc. London. A 301, 359–373.

Kaus, B.J.P., Steedman, C., Becker, T.W., 2008. From passive continental margin to mountain belt: insights from analytical and numerical models and application to Taiwan. Phys. Earth Planet. Inter. 171, 235–251.

King, S.D., Masters, G., 1992. Scott D. King x and Guy Masters. Geophys. Res. Lett. 19, 1551–1554.

Kronbichler, M., Heister, T., Bangerth, W., 2012. High accuracy mantle convection simulation through modern numerical methods. Geophysical Journal International 191, 12–29.

URL: http://dx.doi.org/10.1111/j.1365-246X.2012.05609.x, doi:10.1111/j.1365-246X.2012.05609.x.

Lallemand, S., Heuret, A., 2017. Subduction zones parameters . doi:10.1016/B978-0-12-409548-9.09495-1.

Lawton, T.F., 2019. Laramide sedimentary basins and sediment-dispersal systems. doi:10.1016/B978-0-444-63895-3.00013-9.

Lee, C.T.A., Lenardic, A., Cooper, C.M., Niu, F., Levander, A., 2005. The role of chemical boundary layers in regulating the thickness of continental and oceanic thermal boundary layers. Earth Planet. Sci. Lett. 230, 379–395.

Lenardic, A., Moresi, L., Mühlhaus, H., 2000. The role of mobile belts for the longevity of deep cratonic lithosphere: The crumple zone model. Geophys. Res. Lett. 27, 1235–1238. doi:10.1029/1999GL008410.

Lenardic, A., Moresi, L.N., Mühlhaus, H., 2003. Longevity and stability of cratonic lithosphere: Insights from numerical simulations of coupled mantle convection and continental tectonics. J. Geophys. Res. Solid Earth 108, 1–15. URL: http://doi.wiley.com/10.1029/2002JB001859, doi:10.1029/2002JB001859.

Manea, V.C., Marta, P.G., Manea, M., 2012. Chilean flat slab subduction controlled by overriding plate thickness and trench rollback. Geology 40, 35–38. doi:10.1130/G32543.1.

Meulenkamp, J.E., Kováč, M., Cicha, I., 1996. On Late Oligocene to Pliocene depocentre migrations and the evolution of the Carpathian-Pannonian system. Tectonophysics 266, 301–317. doi:10.1016/S0040-1951(96)00195-3.

Molnar, P., Atwater, T., 1978. Interarc spreading and cordilleran tectonics as alternates related to the age of subducted oceanic lithosphere. Earth and Planetary Science Letters 41, 330–340.

Montési, L.G.J., 2013. Fabric development as the key for forming ductile shear zones and enabling plate tectonics. J. Struct. Geol. 50, 254–266.

Naliboff, J.B., Conrad, C.P., Lithgow-Bertelloni, C., 2009. Modification of the lithospheric stress field by lateral variations in plate-mantle coupling. Geophysical Research Letters 36. doi:10.1029/2009GL040484.

O'Driscoll, L.J., Humphreys, E.D., Saucier, F., 2009. Subduction adjacent to deep continental roots: Enhanced negative pressure in the mantle wedge, mountain building and continental motion. Earth Planet. Sci. Lett. 280, 61–70.

Paul, J., Conrad, C.P., Becker, T.W., Ghosh, A., 2023. Convective self-compression of cratons and the stabilization of old lithosphere. Geophys. Res. Lett. 50. doi:10.1029/2022GL101842.

Pearson, D.G., Scott, J.M., Liu, J., Schaeffer, A., Wang, L.H., van Hunen, J., Szilas, K., Chacko, T., Kelemen, P.B., 2021. Deep continental roots and cratons. doi:10.1038/s41586-021-03600-5.

Rolf, T., Tackley, P.J., 2011. Focussing of stress by continents in 3D spherical mantle convection with self-consistent plate tectonics. Geophys. Res. Lett. 38. doi:10.1029/2011GL048677.

Sandiford, D., Brune, S., Glerum, A., Naliboff, J., Whittaker, J.M., 2021. Kinematics of Footwall Exhumation at Oceanic Detachment faults: Solid-Block Rotation and Apparent Unbending. Geochemistry, Geophys. Geosystems 22, 1–12. doi:10.1029/2021GC009681.

Sdrolias, M., Müller, R.D., 2006. Controls on back-arc basin formation. Geochemistry, Geophysics, Geosystems 7. doi:10.1029/2005GC001090.

Sharples, W., Jadamec, M.A., Moresi, L.N., Capitanio, F.A., 2014. Overriding plate controls on subduction evolution. Journal of Geophysical Research: Solid Earth 119, 6684–6704. URL: https://onlinelibrary.wiley.com/doi/abs/10.1002/2014JB011163, doi:10.1002/2014JB011163.

Sleep, N., Toksöz, M.N., 1971. Evolution of marginal basins. Nature 233, 548–550.

Sternai, P., Jolivet, L., Menant, A., Gerya, T., 2014. Driving the upper plate surface deformation by slab rollback and mantle flow. Earth and Planetary Science Letters 405, 110–118. URL: http://dx.doi.org/10.1016/j.epsl.2014.08.023, doi:10.1016/j.epsl.2014.08.023.

Taramón, J., Rodr?ıguez-Gonza?lez, J., Negredo, A., Billen, M.I., 2015. Influence of cratonic lithosphere on the formation and evolution of flat slabs: Insights from 3-D time-dependent modeling. Geochemistry Geophys. Geosystems 18, 2933–2948. URL: http://linkinghub.elsevier.com/retrieve/pii/S0012821X04004637%5Cn%3CGo to ISI%3E://000167920500003%5Cnhttp://srl.geoscienceworld.org/lookup/doi/10.1785 doi:10.1002/2015GC005940.Received.

Uyeda, S., 1982. Subduction zones: An introduction to comparative subductology. Tectonophysics 81, 133–159.

Wolf, S.G., Huismans, R.S., 2019. Mountain building or backarc extension in ocean-continent subduction systems: A function of backarc lithospheric strength and absolute plate velocities. Journal of Geophysical Research: Solid Earth 124, 7461–7482. doi:10.1029/2018JB017171.

Wortel, M.J.R., Spakman, W., 2000. Subduction and Slab Detachment in the Mediterranean-Carpathian Region. Science (80-.). 290, 1910–1917. URL: http://www.sciencemag.org/cgi/doi/10.1126/science.290.5498.1910, doi:10.1126/science.290.5498.1910.

Yang, T., Gurnis, M., 2016. Dynamic topography, gravity and the role of lateral viscosity variations from inversion of global mantle flow. Geophys. J. Int. 207, 1186–1202.

Yoshida, M., 2012. Dynamic role of the rheological contrast between cratonic

and oceanic lithospheres in the longevity of cratonic lithosphere: A three-dimensional numerical study. Tectonophys. 532, 156–166.

Zhong, S., 2001. Role of ocean-continent contrast and continental keels on plate motion, net rotation of lithosphere, and the geoid. Journal of Geophysical Research: Solid Earth 106, 703–712. doi:10.1029/2000jb900364.

Figure

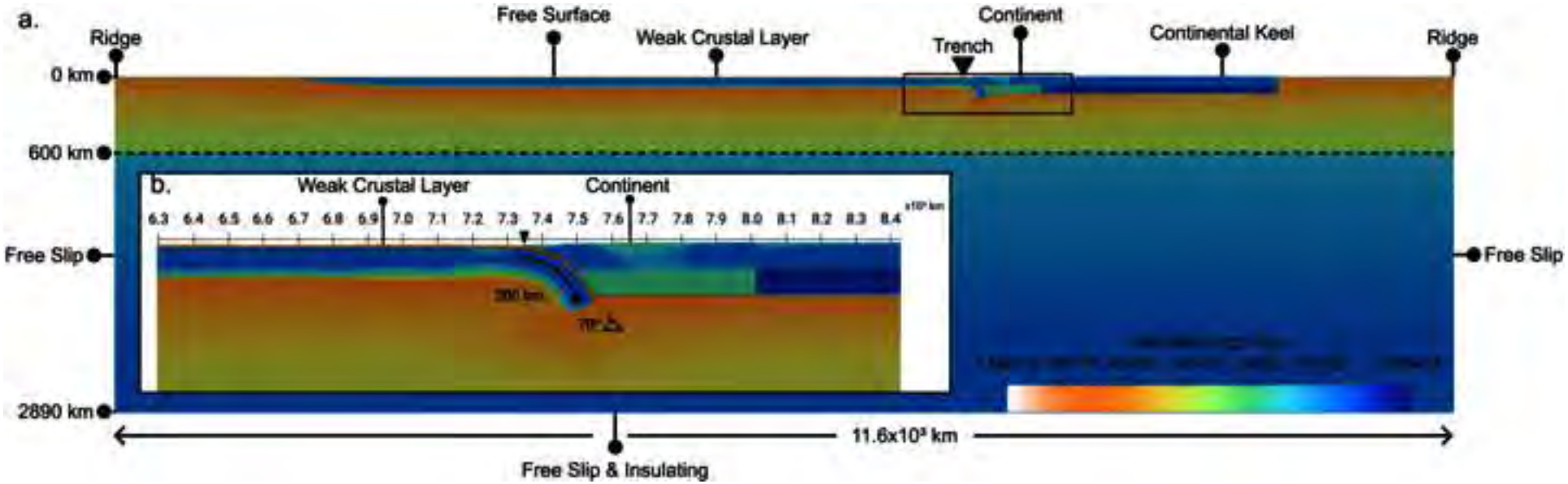

Figure

Click here to access/download;Figure;StrainRates_ConvergenceVel_Margins

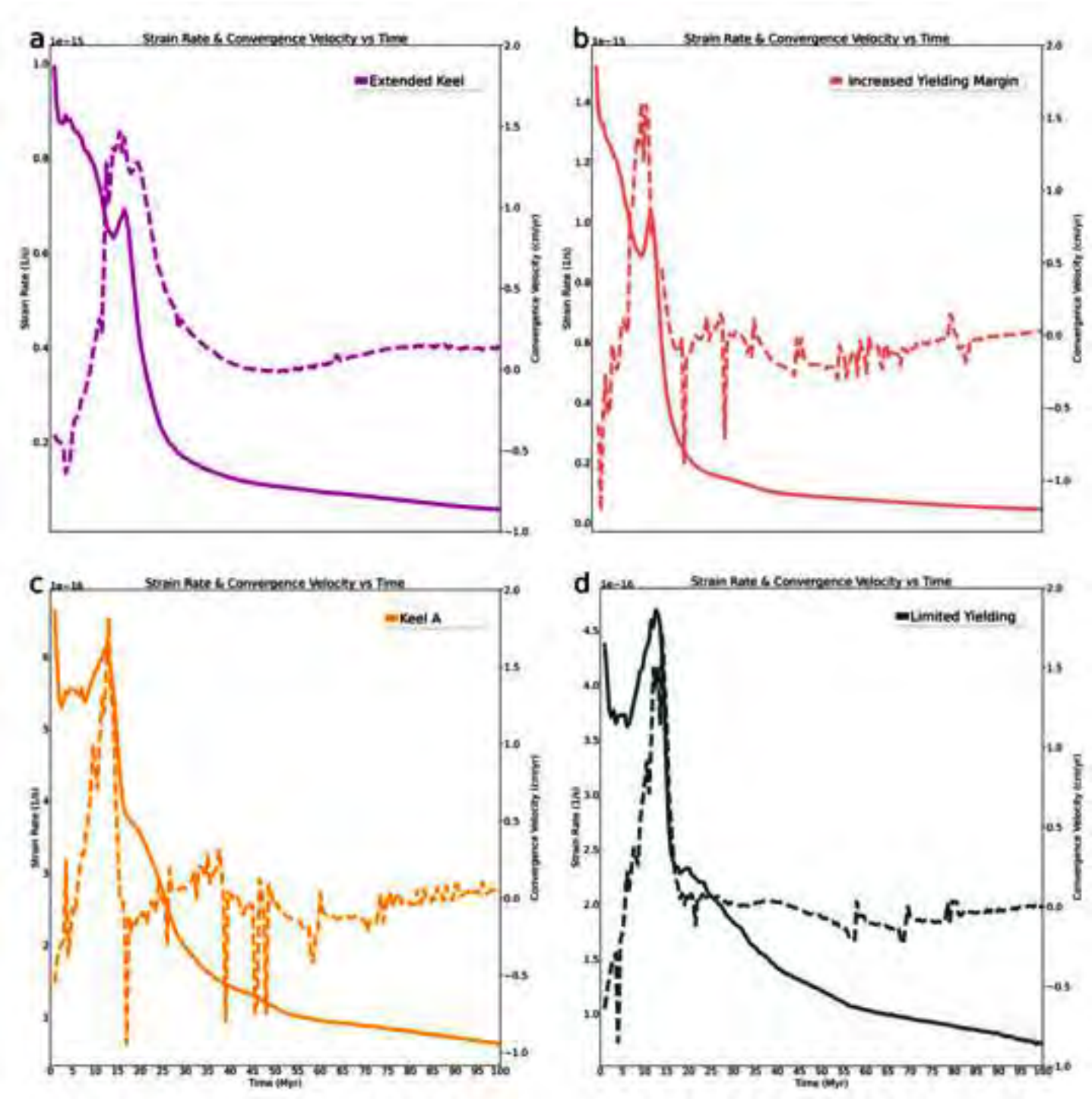

Figure

Click here to access/download;Figure;StrainRate_vs_DeformRegionVel_Margi

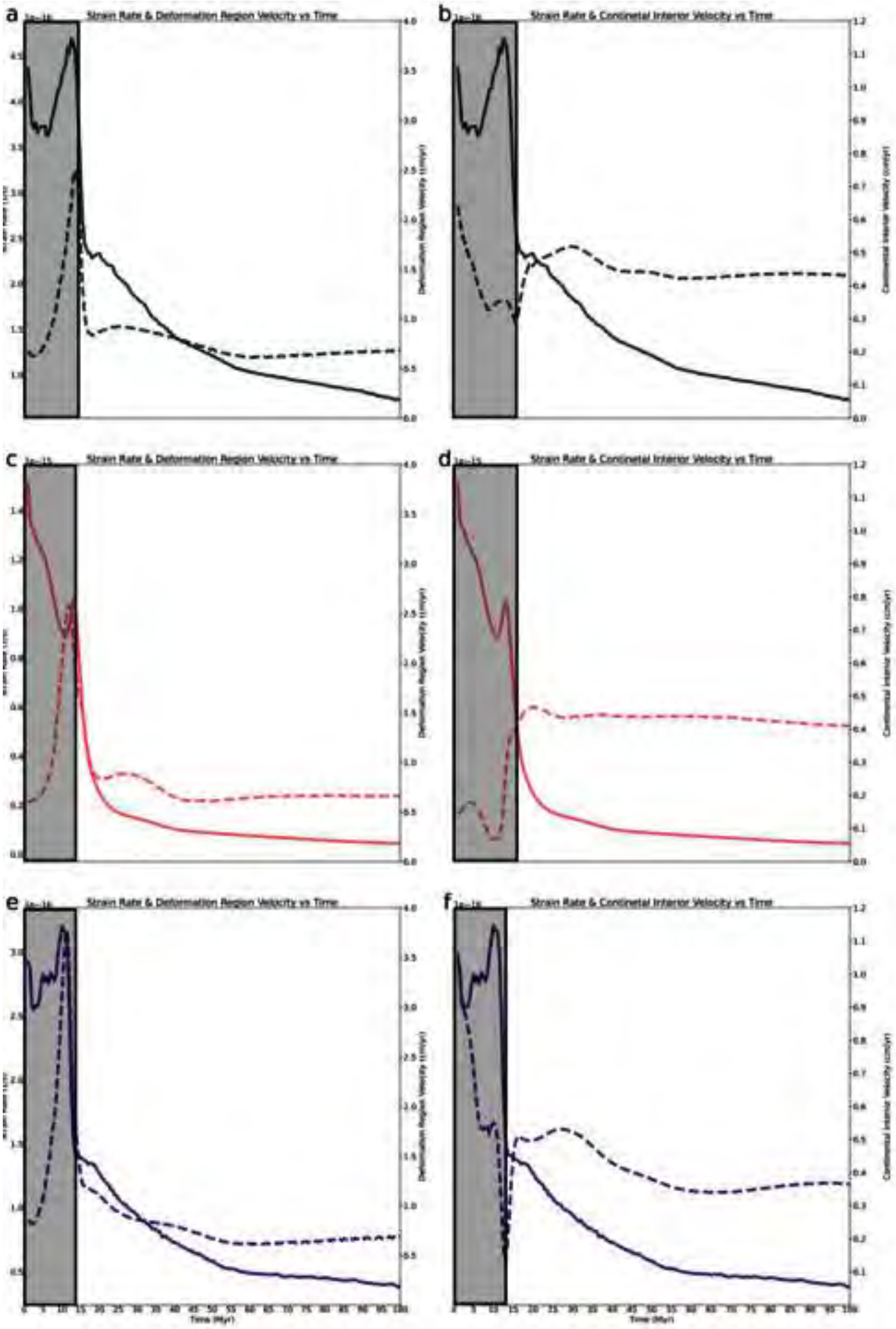

Figure

Click here to access/download;Figure;StrainRate_vs_DeformRegionVel_Keels

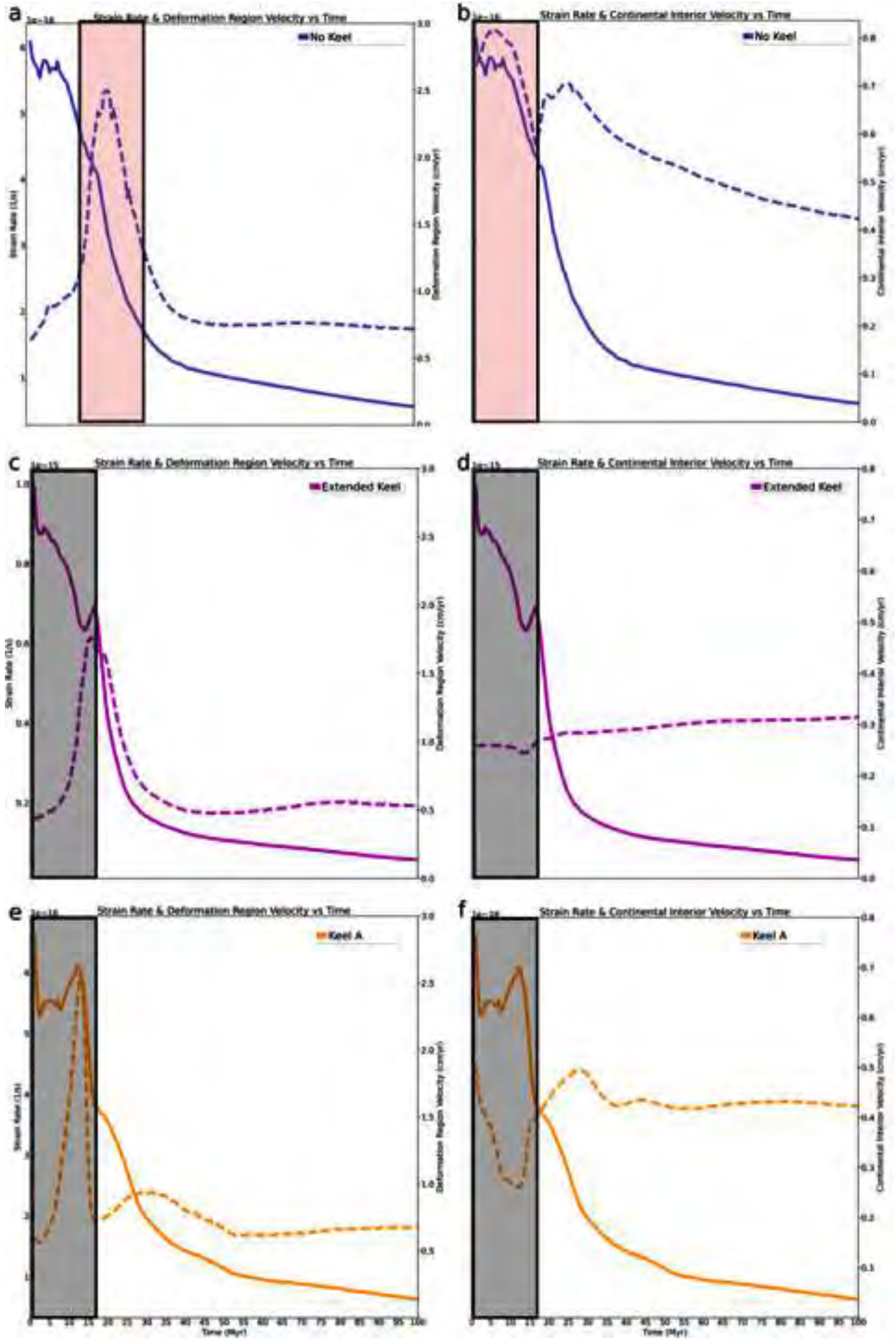

Figure

Click here to access/download;Figure;Topo_Vel_Witharrows_StrainRate_Revi

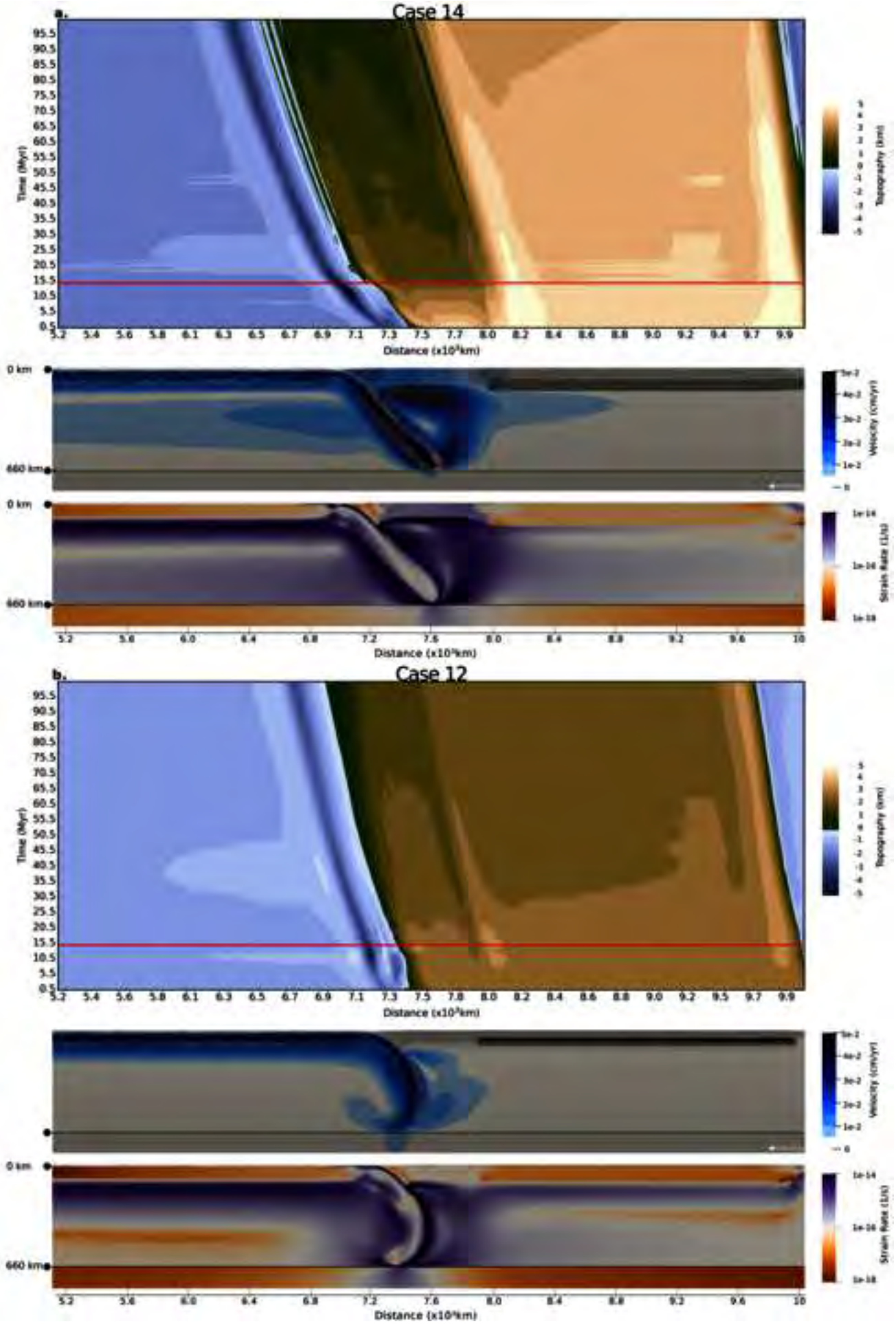

Figure

Click here to access/download;Figure;Margin_Variations_Topo_ETA_VEL_Ge

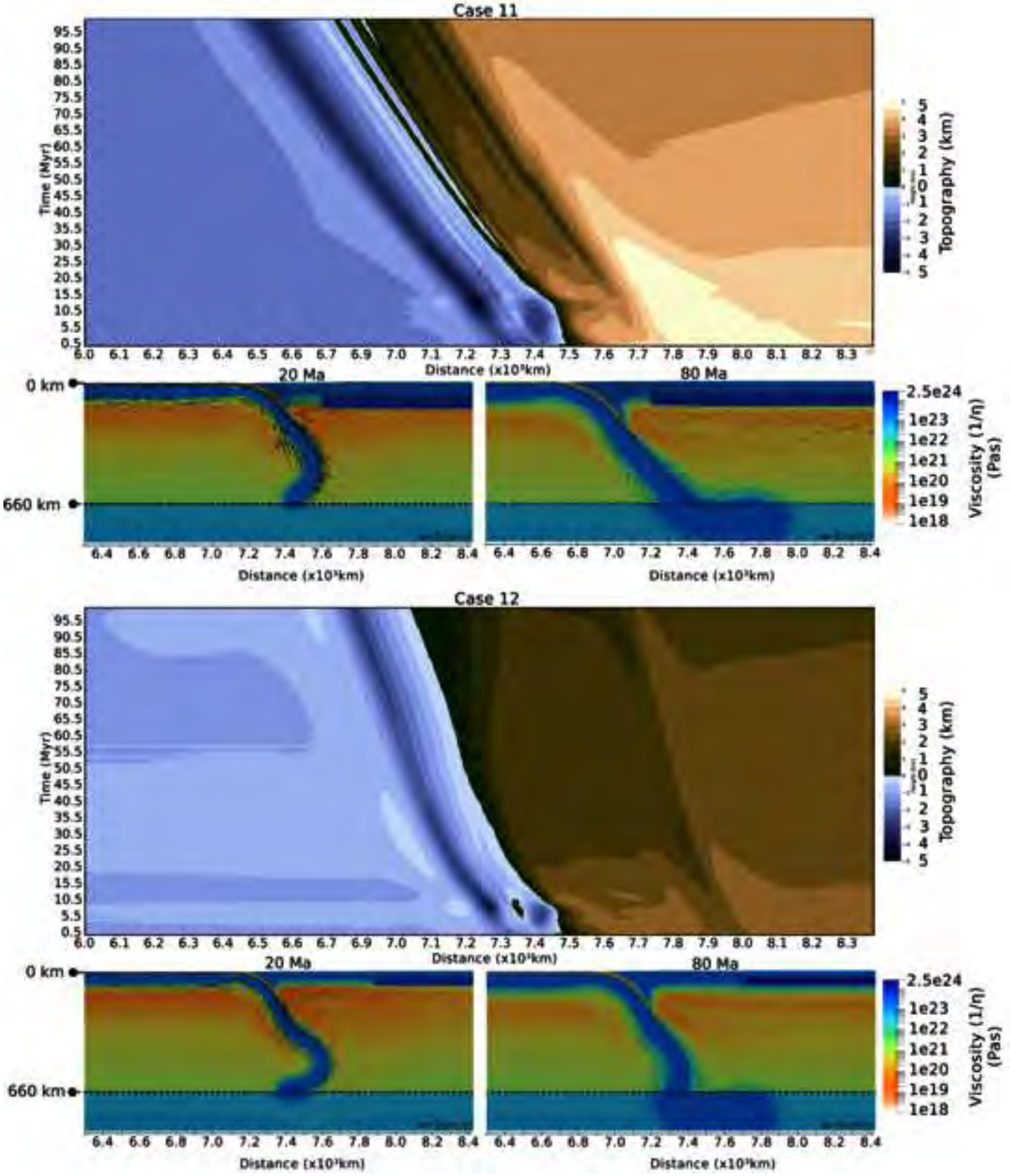

Figure

Click here to access/download;Figure;Margin_Variations_Topo_ETA_VEL_Rh

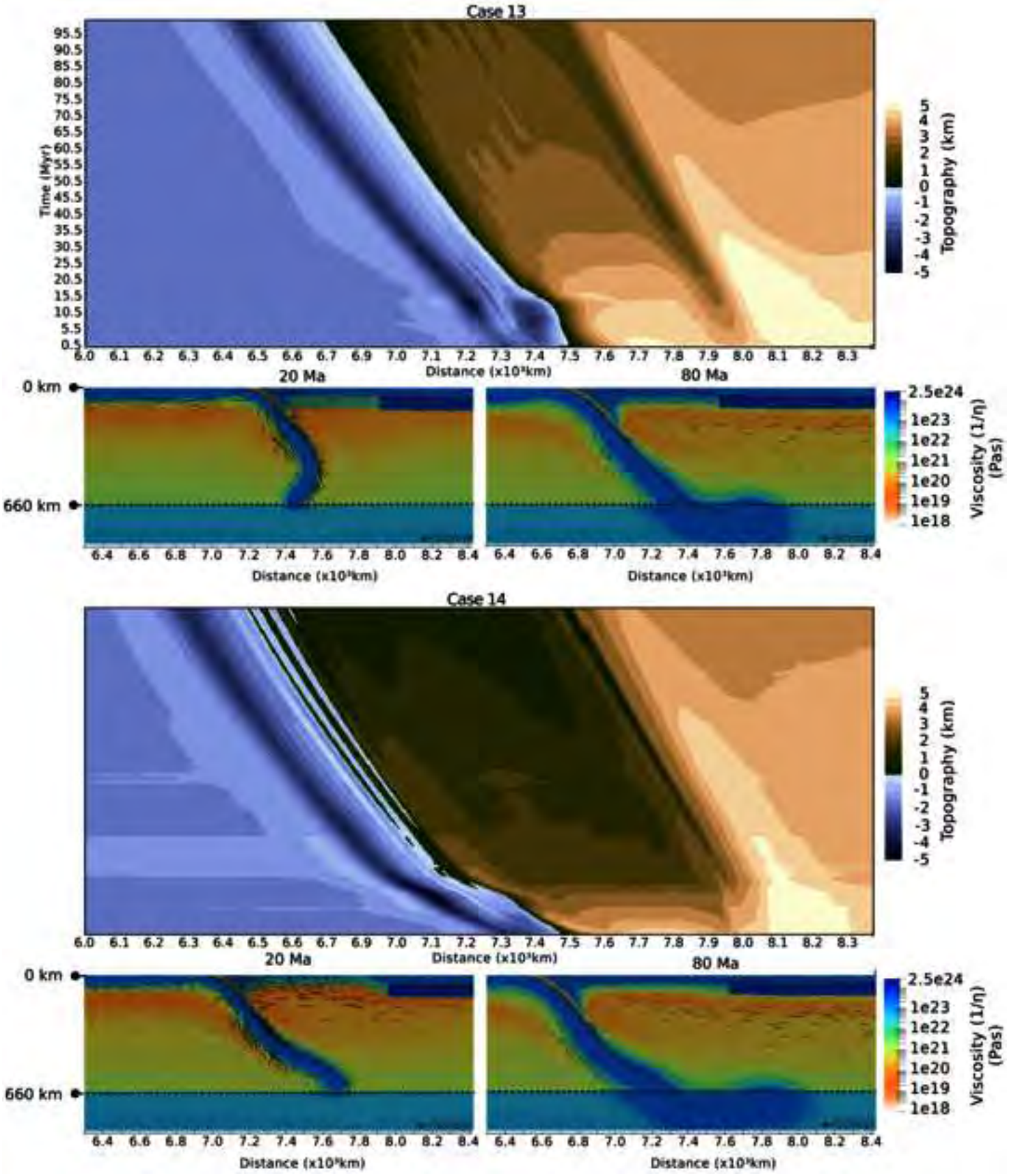

Figure

Click here to access/download;Figure;DeltaDE_DeltaTr_KeelVariation_Revisi

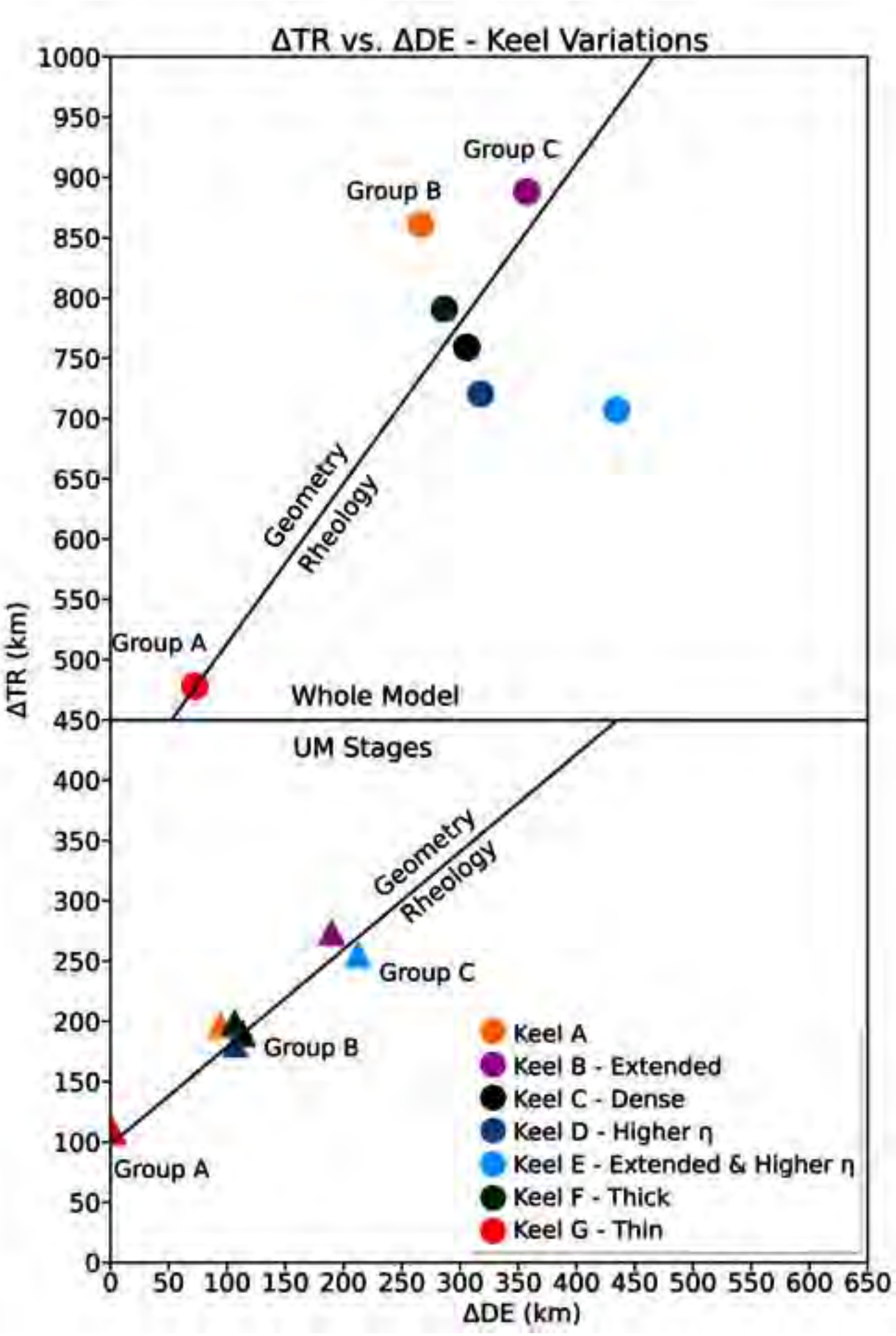

Figure

Click here to access/download;Figure;DeltaDE_DeltaTr_Margin_Variations_R

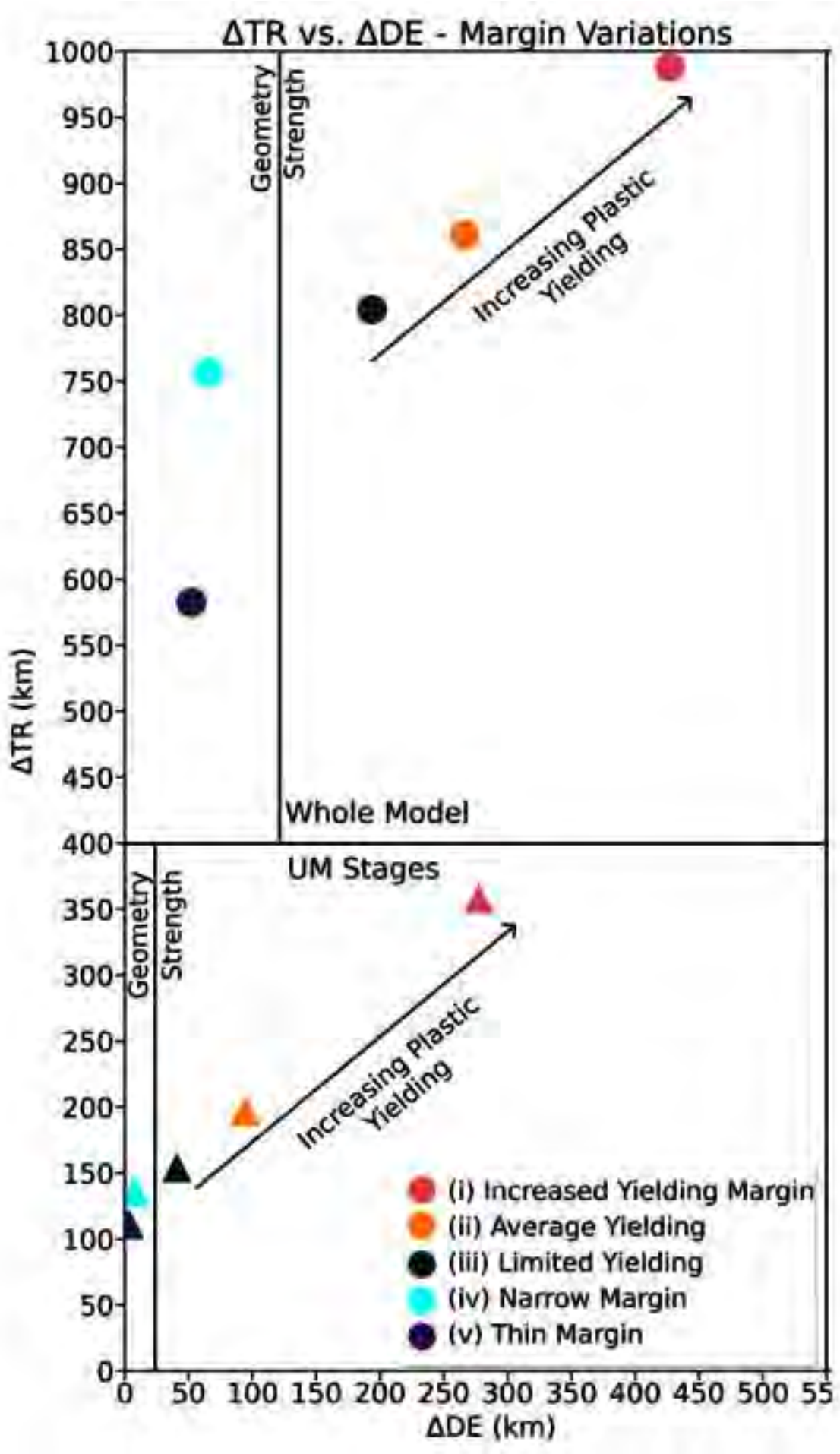

Figure

Click here to access/download;Figure;Mean_StrainRate_DE.png

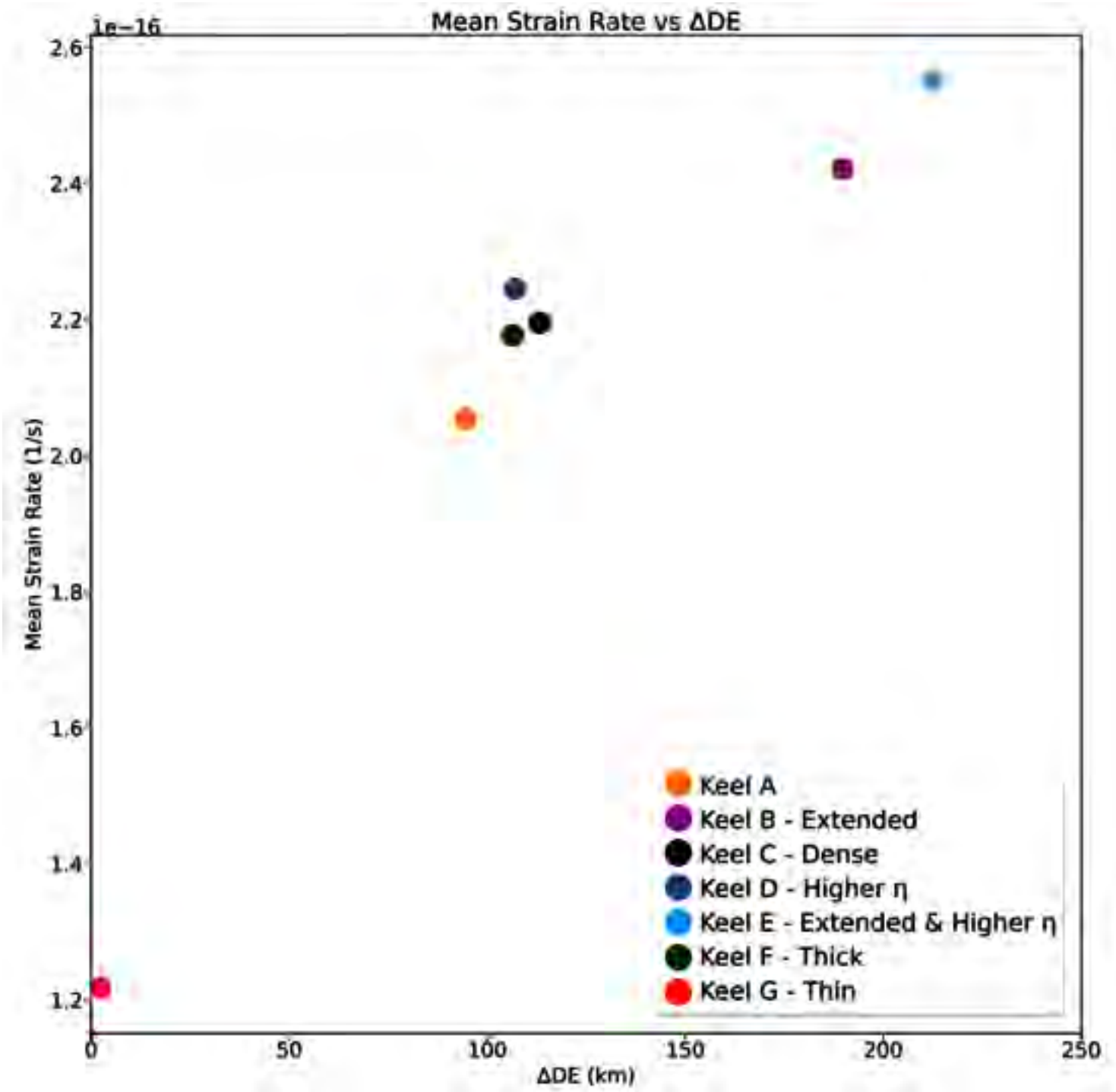

Figure

Click here to access/download;Figure;StrainRates_SubductingPlateVel_NoKe

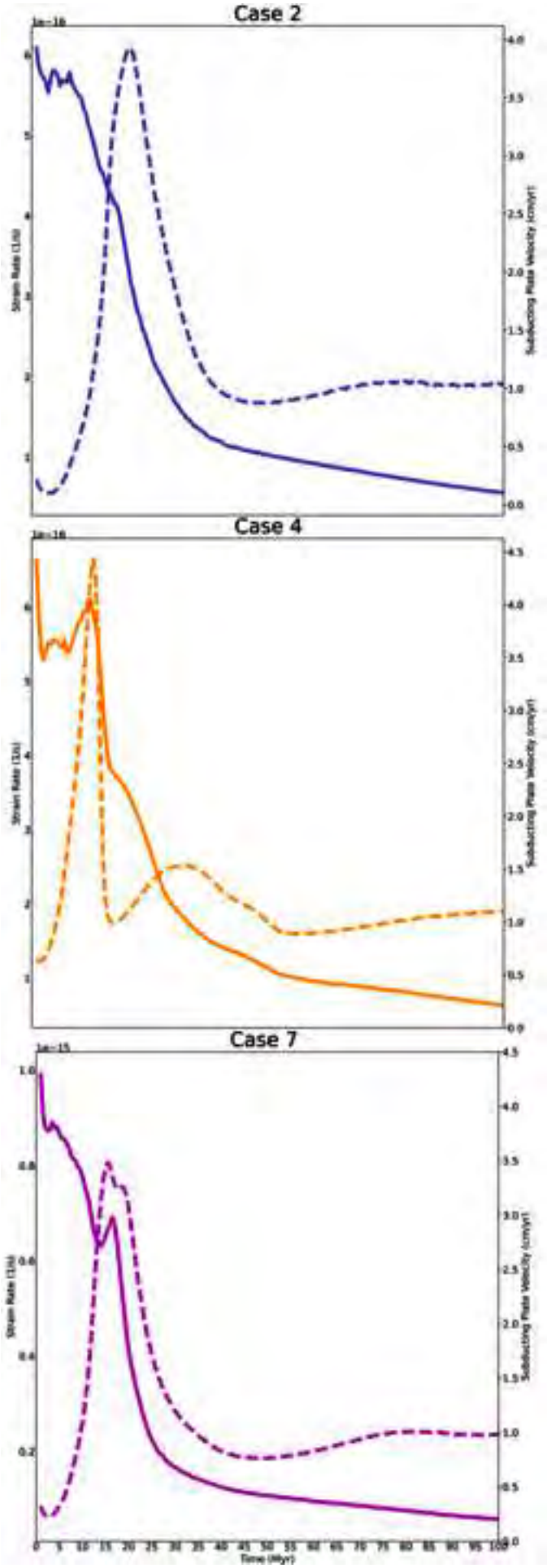

Click here to access/download

Figure (high-resolution)

BC_FreeSlip_FreeSurface_StrongKeelContVertEtaVariations.png

Declaration of interests

☒ The authors declare that they have no known competing financial interests or personal relationships that could have appeared to influence the work reported in this paper.

☐The authors declare the following financial interests/personal relationships which may be considered as potential competing interests: